

Electronic Quantum Coherence in Glycine Molecules Probed with Ultrashort X-ray Pulses in Real Time

David Schwickert¹, Marco Ruberti², Přemysl Kolorenč³, Sergey Usenko^{1,4,†}, Andreas Przystawik¹, Karolin Baev^{1,4}, Ivan Baev⁴, Markus Braune¹, Lars Bocklage^{1,5}, Marie Kristin Czwalinna¹, Sascha Deinert¹, Stefan Düsterer¹, Andreas Hans⁶, Gregor Hartmann⁶, Christian Haunhorst⁷, Marion Kuhlmann¹, Steffen Palutke¹, Ralf Röhlsberger^{1,5}, Juliane Rönsch-Schulenburg¹, Philipp Schmidt⁶, Sven Toleikis¹, Jens Viefhaus⁸, Michael Martins⁴, André Knie⁶, Detlef Kip⁷, Vitali Averbukh², Jon P. Marangos², Tim Laarmann^{1,5*}

¹*Deutsches Elektronen-Synchrotron DESY, Notkestr. 85, 22607 Hamburg, Germany*

²*Department of Physics, Imperial College London, Prince Consort Road, London SW7 2AZ, United Kingdom*

³*Charles University, Faculty of Mathematics and Physics, V Holešovickach 2, 180 00 Praha 8, Czech Republic*

⁴*Department of Physics, University of Hamburg, Luruper Chaussee 149, 22761 Hamburg, Germany*

⁵*The Hamburg Centre for Ultrafast Imaging CUI, Luruper Chaussee 149, 22761 Hamburg, Germany*

⁶*Institute of Physics, University of Kassel, Heinrich-Plett-Str. 40, 34132 Kassel, Germany*

⁷*Faculty of Electrical Engineering, Helmut Schmidt University, Holstenhofweg 85, 22043 Hamburg, Germany*

⁸*Helmholtz-Zentrum Berlin für Materialien und Energie, Albert-Einstein-Straße 15, 12489 Berlin, Germany*

[†]*Present address: European XFEL GmbH, Holzkoppel 4, Schenefeld 22869, Germany*

^{*}**Corresponding author. Email:** tim.laarmann@desy.de

Structural changes in nature and technology are driven by charge carrier motion. A process such as charge-directed reactivity that can be operational in radiobiology is more efficient, if energy transfer and charge motion proceeds along well-defined quantum mechanical pathways keeping the coherence and minimizing dissipation. The open question is: do long-lived electronic quantum coherences exist in complex molecules? Here, we use x-rays to create and monitor electronic wave packets in the amino acid glycine. The outgoing photoelectron wave leaves behind a positive charge formed by a superposition of quantum mechanical eigenstates. Delayed x-ray pulses track the induced electronic coherence through the photoelectron emission from the sequential double photoionization processes. The observed sinusoidal modulation of the detected electron yield as a function of time clearly demonstrates that electronic quantum coherence is preserved for at least 25 femtoseconds in this molecule of biological relevance. The surviving coherence is detected via the dominant sequential double ionization channel, which is found to exhibit a phase shift as a function of the photoelectron energy. The experimental results agree with advanced ab-initio simulations.

Introduction

Inducing and steering the correlated motion of electrons in many-body quantum systems is a cornerstone in photonics and drives technological innovation. In particular, understanding the temporal evolution of electronic coherences, i.e. the dynamics of coupled electronic many-body configurations forming electronic wave packets that propagate in space and time, is one of the grand challenges in ultrafast science. Electronic coherence may well be key to photochemical change in matter, in particular to the onset of radiation damage in a wide range of scenarios, from single-molecule X-ray imaging to radiobiology. Energy transfer can be more efficient and faster if it is guided along a well-defined pathway governed by quantum mechanical wave packet motion. Efficient molecular junctions and molecular transistors rely on charge transport channels with negligible energy dissipation during the carriers' propagation time. Therefore, a mechanistic understanding of subsequent decay processes on the quantum level plays a vital role in the design of future molecular electronics and functional nanostructured devices.

In recent years, intensive debate was stimulated by a seminal study reporting long-lived electronic coherences in polyatomic molecules (1). There, extreme ultraviolet (XUV) pulses ionize the amino acid phenylalanine. Several electronic states are coupled in the cation due to the broad spectral bandwidth of the femtosecond (fs) XUV pulse. Near-infrared pulses probe the initiated coherent dynamics by photofragmentation. The recorded fragmentation pattern shows an oscillatory behavior as a function of pump-probe delay with a time period of 4.3 fs that persists for tens of fs. Matching the corresponding energy difference of relevant energy levels, the results have been interpreted as long-lived electronic coherences. Still, the key interrelated questions are whether the electronic coherence can really be that robust and whether it can be detected directly, i.e. through electronic observables?

By defining charge migration as purely electronic non-equilibrium dynamics of a coherent superposition (interference) of cationic eigenstates following ionization (2), several processes may affect the propagation of the generated electronic wave packet. Inelastic scattering of the outgoing photoelectron may lead to excitation of one or more other bound electrons, which will contribute to the initiated multielectron dynamics. The electronic excitation can rapidly relax into vibrational modes. Beyond the influence of moving nuclei as point-like charges in a classical picture, the quantum dynamics of nuclear wave packets is prone to destroy electronic coherences (3). Theoretical works treating nuclear dynamics classically found that electron hole migration in other prototypical model systems, such as tryptophan (4), benzene (5) and glycine (6) is not significantly perturbed by nuclear motion within the first 20 fs after the excitation. However, a full quantum dynamical treatment suggests that electronic coherence is lost after just a few fs in the case of phenylalanine (3). In these calculations electronic wave packet decoherence is driven by the zero-point nuclear spread (7), that is also at the core of our present theoretical treatment. Up to now, no direct measurements (i.e. such based on the electronic observables) of coherent multielectron dynamics were available to resolve this controversy.

In the present contribution, we monitor the birth and propagation of an electronic wave packet generated in the interaction of fs x-ray pulses with glycine molecules by means of time-resolved electron spectroscopy at the carbon K-edge from a second fs x-ray probe pulse. The analysis of electrons emitted by single photoionization, sequential double photoionization and Auger decay with element specificity and orbital selectivity as well as unprecedented quantum mechanical phase sensitivity is an experimental breakthrough. It probes the transient local electron hole density in inner-valence molecular orbitals directly in the time domain and allows for tracing long-lived electronic coherences that result from the coherent coupling of cationic eigenstates long before fragmentation of the carbon backbone sets in.

Results

Glycine is the simplest of the twenty natural amino acids acting as molecular building blocks of more complex biochemical compounds such as peptides and proteins (8). It contains the characteristic amine (-NH₂) and carboxyl (-COOH) functional groups linked via a methylene bridge and is sketched in the center of Fig. 1B. The neutral molecule has $N = 40$ electrons forming a closed-shell system in its ground state, which can be described by 20 molecular orbitals. A recent theoretical paper reported photoionization cross sections for the different electron orbitals using density functional theory (9). The theoretical results describing the static electronic structure are in good agreement with experimental photoelectron spectra recorded at a synchrotron light source (10). The valence and inner-valence electron orbitals (6a' - 16a', 1a'' - 4a'') exhibit binding energies E_b in the range of approximately (10 - 35) eV (6, 9, 10).

In our time-resolved experiments we used a single-color, femtosecond x-ray pump-probe technique (11, 12). The charge carrier dynamics were initiated by free-electron laser (FEL) pulses of a few-fs duration at the central photon energy of 274 eV. Whereas the photon energy was sufficient to ionize electrons from all valence and inner-valence orbitals, the localized 1s core electrons of carbon (~284 eV), nitrogen (~400 eV) and oxygen (~532 eV) were not accessible. The FEL pulses were focused onto the molecular beam produced from glycine powder heated to 160 °C. Electrons generated at the intersection volume were detected with a magnetic bottle electron spectrometer. More details on the experimental setup can be found in the methods section.

First, we measured the kinetic energy E_{kin} of emitted electrons as a function of FEL photon energy $E_{FEL} = h \cdot \nu$ tuned below the carbon K-edge (13). Fig. 1A shows the recorded kinetic energy distributions, comprising contributions from the initial photoelectron emission, the subsequent Auger decay channel opened by the x-ray probe

pulse excitation of localized carbon 1s electrons and probe-induced photoionization of singly charged glycine cations. Emission bands originating from prompt photoionization of valence and inner valence orbitals of the neutral molecule with binding energies E_b shift in their kinetic energy according to $E_{kin} = h \cdot v - E_b$. The overall width of the distribution is ~ 25 eV in agreement with the published data (9, 10). Additional electron emission bands are observed that do not shift as a function of photon energy. These electrons originate from the probe-induced Auger decay, as their kinetic energy is solely given by the electronic structure of glycine molecules. A competing ionization channel resulting in doubly charged glycine ions is the probe-induced photoemission of valence electrons from the initially formed cation. The low-energy onset of their kinetic energy distribution is shifted towards lower energy by the 2nd ionization potential (22 eV) as indicated in Fig. 1A. Note the high-energy tail of the kinetic energy distribution may still reach the upper limit taking into account photoelectron emission from electronically excited cations. In the following we discuss the overall coherent electron dynamics tracked in the present time-resolved experiments. The total cascade involves several different processes: (1) photoionization, (2) charge migration and (3a) resonant carbon 1s core-hole excitation followed by Auger decay or (3b) sequential double photoionization of glycine depicted in Fig. 1B.

Upon photoionization with femtosecond x-ray pulses we generate electronically excited many-body states in the glycine cation (14). At the central photon energy of 274 eV, which corresponds to the x-ray wavelength of 4.5 nm, the FEL spectral bandwidth below 0.45% full width at half maximum is sufficient to coherently couple several cationic eigenstates. Details on the longitudinal coherence properties of the applied single-mode FEL pulses can be found in the literature (15, 16) and in the methods section. The ionization paths leading to the same photoelectron energies but leaving behind different cationic states interfere and trigger coherent quantum motion of the remaining $N-1$ electrons of the cation. The induced electronic dynamics depend on the

involved eigenstates. In the present study, we focus mainly on photoelectron emission from the 10a' molecular orbital visualized in the center of Fig. 1B with a binding energy of ~ 20 eV. Ionization results in essentially two cationic eigenstates Ψ_α and Ψ_β , each with $\sim 50\%$ contributions from the inner valence hole (1h) state and $\sim 50\%$ of a series of excited two-hole one-particle (2h1p) configurations (17). In the latter an additional bound valence electron is excited due to electron correlation. The time-dependent electronic wave packet describing the motion of the positive charge created in the photoionization step as a function of time t can be written in simple terms as a linear combination:

$$\Psi^{N-1}(t) = c_\alpha e^{-iE_\alpha t} \Psi_\alpha + c_\beta e^{-iE_\beta t} \Psi_\beta \quad (1)$$

with expansion coefficients c_α, c_β . In this picture the positive charge oscillates with a time period T given by the energy separation of the two involved eigenstates, where \hbar is Planck's constant over 2π :

$$T = \frac{2\pi\hbar}{|E_\alpha - E_\beta|} \quad (2)$$

The $N-1$ electron density integrated over all electron coordinates but one oscillates with the same time period due to constructive and destructive interference of mixed states contributing in equation (1), i.e. due to the character of the Ψ_α, Ψ_β doublet in glycine with almost equal 1h state contribution each (17). The fate of the positive charge in the molecular skeleton can in principle be followed in several different ways. On the one hand, the transient electron hole states are probed by excitation of a strongly localized carbon 1s core electron into the 'empty' electron-hole state via time-delayed fs x-ray pulses of the same color (17). As long as the electronic coherence, i.e. the electronic wave packet described by equation (1) is preserved, the resonant x-ray transition (1s \rightarrow 1h) fills the inner-valence orbital and produces a carbon 1s core hole with high efficiency. The probability of the core 1s to inner-valence hole transition depends on the time-dependent

amplitude of the cationic 1h-state localized on the carbon atom. The corresponding yield is a direct measure of the transient electron configuration mixing. The theoretically predicted oscillation period T is (10 - 20) fs (17-19). Thus, the induced coherent electron dynamics following 10a' photoionization can be observed directly by recording the subsequent Auger electron emission as a function of x-ray pump – x-ray probe time delay. The basic experimental scheme flanked by ab initio simulations has been proposed by Cooper et al. (17) already in 2014. On the other hand, the electron dynamics is also monitored by photoelectron emission from sequential double photoionization processes. This turns out to be the dominant process (by a factor 10) in our measurements although contributions from the first process will be present in the data.

Here, we report the first-ever direct observation of the complex and evasive phenomenon of ultrafast electronic coherence and charge migration occurring in ionized glycine molecules by means of time-resolved electron spectroscopy with single-digit femtosecond precision. In recent work the resonant probing (X-ray absorption) scheme was used to probe a transient hole state in isopropanol, in that case faster decoherence eliminated the observation of oscillations (20). In the present joint experimental and theoretical work, we present the full quantum dynamical picture supported by advanced calculations solving the time-dependent Schrödinger equation for the x-ray-driven multielectron quantum system (for details see supplementary information).

Fig. 2A shows the result on a 25-fs time scale. Here, we counted the electrons with kinetic energies in four different ranges determined by the FEL spectral bandwidth: (i) from 259 to 263 eV, (ii) 252 to 256 eV, (iii) 235 to 239 eV and (iv) 231 to 235 eV and plotted the relative change of the electron yield in each energy bin (i-iv) as a function of pump-probe delay in 1 fs steps. Oscillations of the detected electron signal in the time domain are clearly visible. The curves for high-energy and low-energy electron emission show a π phase shift with respect to each other, i.e. the electron yield in different energy

ranges is maximized/minimized for different x-ray pump-probe delays as shown in Fig. 2B. In order to work out for which electron kinetic energy the quantum phase jump occurs, the delay dependent electron spectra have been fitted in steps of 1 eV with sinusoidal functions and a 4-eV detection range keeping the oscillation period, amplitude and phase of the quantum beat as free parameters (see methods section). The outcome is summarized in the Fig. 2C-F. We observe the π -phase jump at an electron kinetic energy of (246 ± 2) eV. Above and below this transition the relative change of the detected electron yield oscillates with a time period of $T = (19.6^{+2.2}_{-1.4})$ fs over the full kinetic energy range of Auger electron emission from 224 to 264 eV indicated by the red shaded area in Fig. 1A. It is important to note that probe-induced Auger decay leads to the same final quantum states with two electron holes in the valence band as sequential double ionization (see Fig. 1A, right columns). Hence, in a rigorous theoretical treatment the detected quantum path interference, i.e. amplitude and phase of the observed oscillation, is given by the coherent sum of all contributing probe-induced ionization channels. In any case, its time period is given by the beating frequency of the cationic eigenstates Ψ_α, Ψ_β because the initial photoionization from 10a' leaves behind the cation in the nonstationary superposition of Ψ_α and Ψ_β that interfere according to equation (1) and determine the corresponding transition dipole moments and phases.

We have simulated the experimental observables using the measured FLASH pulse parameters and including the various ionization channels. The numerical ab-initio result on the probe-induced electron-yield modulation in pump-ionized glycine molecules as a function of x-ray pump-probe delay is summarized in the Fig. 3A-C. Our theoretical simulations show that the observed phase jump is not caused by the interference between Auger and sequential double ionization channels and instead is a property of the sequential double ionization alone, see further details in the supplementary information. Both channels monitor the same beating frequency of the cationic eigenstates. However, sequential double ionization is dominant (by a factor of 10 at least) over the Auger decay

for the laser parameters used in the experiment and specifically for the carbon core holes in this molecule. A deeper analysis of the resulting kinetic energy spectrum of electrons clearly shows that the phase jump is present only because of the sequential double ionization channel itself. The calculated signal is different from and goes beyond the primitive survival probability of the initial cationic superposition state. In fact, time-dependent B-spline restricted correlation space (RCS) – algebraic diagrammatic construction (ADC) simulation code (21-23) provides the populations, degrees of coherence and relative phases between each pair of accessible cationic states computed using the ADC(2,2) method (24), as well as the relative change of electron kinetic energy spectra as a function of pump-probe time delay as recorded in the measurements. The simulation code combines the accurate description of the photoelectron continuum by means of the B-spline basis set (25) and the ADC description of electron correlation. The agreement between experiment and theory fully supports the data interpretation of an electronic coherence induced and tracked in real time by ultrashort x-ray pulses. The amplitude of the observed oscillation reflects the strength of the initial 10a' photoionization channel, see further details in section S2.2 and Fig. S3 in the supplementary information.

We note that the calculated binding energies of cationic eigenstates are not exact and may easily be off by up to \sim 10 eV, because in ab-initio calculations the absolute energies of states are always significantly less accurately determined than the relative energies. Therefore, we plot the simulated time-dependent electron spectra presented in Fig. 3B and Fig. 3C relative to the theoretically derived phase jump energy (\sim 255) eV, which is above the observed experimental value of (246 ± 2) eV. Furthermore, the ionization dynamics for pump-probe time delays of a few fs where the x-ray pulses strongly overlap cannot be accurately described in our model. The reason is that theoretically the pump and probe simulations are carried out independently and the probe simulation assumes that the pump-induced ionization is completed. This is also the reason

why the onset of the observed electron-yield oscillation slightly differs between experiment and theory. We also note that according to theory the Auger spectra as well as the sequential double ionization spectra do not significantly depend on whether the inner-valence hole is located on the carbon atom bridging to the amine group or on the carboxyl group itself (see supplementary information). Although the resonant $4a' \rightarrow 9a'$ transition energy for inner-shell excitation of the carboxyl group is close to the FEL photon energy and therefore considered in the simulation, the FEL spectral bandwidth of less than 1.2 eV (FWHM) is too small to coherently couple the two C1s core orbitals $4a'$ and $5a'$ with high efficiency. Their relative chemical shift is of the order of 2.9 eV, which gives a time period of ~ 1.4 fs for the corresponding quantum beat that cannot be resolved in the present experiment. Nevertheless, the contribution from adjacent $9a'$ configurations to the observed dynamics in the dominant sequential double ionization channel is fully taken into account in our simulation.

To identify the somewhat weaker resonant Auger channel experimentally demonstrating the element specificity and orbital selectivity of the $1s \rightarrow 1h$ resonant transition, we selected FEL shots in which two electrons were detected in coincidence. Out of $\sim 6 \times 10^5$ electrons created in the interaction of glycine molecules with $\sim 1 \times 10^8$ FEL pulse pairs we identified ~ 7600 coincidences integrated over all time delays (see methods section). In Fig. 4 the kinetic energy of the first (faster) and second (slower) electron are plotted on the x- and y-axis, respectively. Among the many possible multielectron excitation pathways and decay channels creating doubly charged final states, particularly those cascades starting with photoionization of the $9a'$ and $10a'$ molecular orbitals are significantly enhanced in the coincidence map as indicated in Fig. 4.

We see that the time-resolved electron spectroscopy with x-rays is particularly sensitive to the changing local electronic structure, i.e. the transformation of electronic

orbitals. However, nuclear motion affecting the coherence of the electron-hole survival probability in time domain cannot be completely excluded, because the solution of the time-dependent Schrödinger equation given in equation (1) depends also on nuclear coordinates. Note, that the oscillation in the electron yield is observed even without selecting a specific conformer. At an average oven temperature of 160 °C in our gas phase experiment only two conformers commonly referred to as Gly I and Gly III are expected to contribute to the molecular response at a ratio of approximately 2:1 (17, 26). Theoretical investigations have shown that the ionization out of orbital 10a' gives rise to different charge carrier dynamics in Gly III and Gly I with timescales varying from about 10 to 20 fs, respectively (19). Small variations in the initial nuclear positions lead to noticeable dynamic changes (6). Therefore, the time-resolved electron spectroscopic data presented here gives the effective oscillation period T for the mix of conformers present in the molecular beam. Recent theoretical work on the role of coupled electron-nuclear dynamics induced by broadband attosecond XUV pulses found that charge carrier dynamics in glycine molecules is barely affected by nuclear motion or non-adiabatic effects during the first 5 - 10 fs, and that the initial electronic coherences do not dissipate at least during the first 20 fs (6). We would like to emphasize that the computational demands of the B-spline RCS-ADC method prevent to take into account the nuclear part of the wave function. However, by a computationally cheaper simulation of the survival probability of the pump-prepared ionic density matrix, which included the initial zero-point nuclear geometry spread of the molecule calculated using the Molpro quantum chemistry software package (27), we have shown that the oscillations survive this averaging and are discernible over at least 25 fs. The fact that the oscillations survive this averaging is an important aspect. It is far from a-priori obvious and in some molecular state superpositions it won't (for details see supplementary information).

Discussion

The key finding of the present work is that the detected electron-yield oscillation monitoring the quantum wave packet dynamics of the remaining positive charge in the glycine cation exhibits the opposite phase in the dominant sequential double ionization channel depending on the kinetic energy of emitted electrons. This is a purely electronic effect and the ultimate confirmation of the excited electronic coherence. The kinetic energy where the π phase jump occurs is solely determined by the transient electronic structure of the cation. The resulting time-dependent modulation of the electron yield can be fitted with a sinusoidal function of the same time period $T = (19.6^{+2.2}_{-1.4})$ fs shifted by π (see methods section). The oscillation can be either imprinted on the Auger yield or on the sequential double ionization yield. The mechanism is the same, interference of the transition from two or more coherently populated initial ionic states into the same final continuum state. In the language of coherent multidimensional spectroscopy, the first x-ray pulse creates an electronic coherence, and the second pulse efficiently projects it into a population of interfering continuum states and a superposition of cationic eigenstates, respectively. We note that multidimensional nonlinear x-ray spectroscopy signals have been recently simulated to study valence excited state wave packets in core-ionized glycine molecules (28). This and other theoretical studies illustrate the power and potential of modern x-ray FEL sources, where electronic coherences can be probed unambiguously and with unprecedented sensitivity (29-31). It was shown that even under influence of nuclear dynamics in complex polyatomic molecules, the coherence evolving in the non-Born–Oppenheimer dynamics of several electronic states can survive for much longer than the timescales investigated in the present work (31).

The phase shift in the dominant sequential double ionization channel of glycine is fully reproduced in our many-electron time-dependent simulation and is a result of interference of dipole transitions from the coherently populated singly ionized states of

glycine into the double ionization continuum, see Eq. (5) of (18). Our study provides benchmark information on the complex many-electron physics underlying charge migration in the amino acid glycine. We monitored how the charge distribution changes in this biological building block of nature in real-time. We saw the full motion picture of the non-stationary electronic states formed in the glycine cation for 25 fs and have reached an understanding of the migration process on the quantum level of electrons and holes, respectively. During its propagation the initially prepared ‘pure’ electronic non-stationary state in the cation did not evolve towards a statistical mixture mediated by the coupling to nuclear degrees of freedom. One may have expected from theoretical studies of electronic decoherence phenomena in other molecules that the nuclear quantum wave packets moving on the coherently coupled potential surfaces (electronic states) quickly lose overlap, the population of the coupled electronic states immediately changes and dephasing of the electronic wave packet due to different phase velocities of the participating partial waves destroys the electronic quantum coherence rapidly and irreversibly within a few femtoseconds (3, 7). Our direct electron-detection-based observation shows that for inner-valence charge migration in glycine, this is not the case. The electronic quantum coherence in this complex system exists for at least 25 fs. Our observation provides a direct experimental confirmation for the fascinating idea of electronic coherences persisting for many 10’s of femtoseconds supporting energy transfer and charge separation in quantum transport phenomena in biological molecules and opens up new vistas for steering such processes with coherent light (32).

Materials and Methods

Experimental Design. The experiment was carried out at the FL24 beamline of the FLASH2 free-electron laser (FEL) at DESY in Hamburg (13). The FEL is operated in 10 Hz bursts with trains of 400 electron bunches each with 1 μ s separation, in a special short pulse mode with low electron bunch charge of a few tens of pC. Each bunch

generates a coherent FEL pulse with sub-5 fs duration at 274 eV photon energy and an average pulse energy of about 5 μ J (4000 photon pulses per second in total). The FEL wavelength is tuned by changing the gap between the magnetic poles of the FEL undulator magnets, while the electron beam energy is kept constant at 1.24 GeV. The scheme of the experimental setup is shown in Fig. 5.

We used a split-and-delay unit consisting of two interleaved lamellar mirrors in the unfocussed beam to generate two replicas of collinearly propagating FEL pulses with a controllable delay (12). The resulting pump-probe sequences were focused into the interaction region by a toroidal mirror with a focal length of about 5.7 m. Both, the lamellar mirror pair and the focusing mirror were nickel coated and operated at 8° angle of incidence to the surface.

For the experiments, >98.5% glycine was acquired from Sigma-Aldrich and used without further purification. The glycine molecules were delivered to the interaction region by evaporation of glycine powder at 160 °C in a resistively heated oven. The resulting vapor pressure of glycine in the 10^{-3} mbar range produced an effusive beam of sufficient density.

The photoelectrons and Auger electrons generated in the interaction region were detected by a microchannel plate (MCP) detector in a magnetic-bottle type time-of-flight (TOF) electron spectrometer. It allows the application of retardation fields to provide the necessary resolution for fast electrons with several hundred eV kinetic energy. The MCP signal was digitized by a fast analog-to-digital converter and stored in the FLASH data acquisition system. The electron kinetic energies were calibrated with the well-known photoelectron spectrum of argon.

To generate the shortest possible pulses FLASH uses a separate photoinjector laser optimized for low bunch charge operation. The low charge enables a very high bunch compression due to smaller space charge effects. The short electron bunch reduces the number of individual longitudinal modes present in the FEL pulses, in the ideal case

down to a single mode. This is referred to as single-spike SASE or single-mode SASE operation. It increases the longitudinal coherence as the slippage between the electrons and the light in the undulator is larger than the bunch length so the light emitted from the tail of the electron bunch reaches the head of the bunch within a few gain lengths and clearly before saturation. Single-spike operation delivers sub-5 fs pulses with a high degree of longitudinal coherence from a SASE source as the whole electron bunch interacts with the light from the same mode (15, 16).

During our beamtime we used the Online Photoionization Spectrometer (OPIS) system in the FLASH2 tunnel for photon diagnostics (13). OPIS consists of four electron time-of-flight spectrometers arranged in a cross shape to monitor the FEL wavelength and bandwidth by detecting photoelectrons from a thin rare gas target. In order to evaluate the FEL spectral bandwidth we correlated events in which two electrons were detected in opposite lying TOF spectrometers. Each photoelectron was assigned to either the Argon $2p_{1/2}$ or $2p_{3/2}$ orbitals and only matching pairs originating from the same orbital of two atoms within one FEL shot were considered. It results in a total number of $\sim 2.6 \times 10^7$ electron pairs plotted in Fig. 6. For these pairs, the differences of their respective photoelectron kinetic energies were calculated and are shown as a histogram. The width of the equidistant energy bins was chosen to approximate the resolution of the analog-to-digital converter with a sampling rate of 7 GHz. This procedure results in an autocorrelation of the FEL shots in the spectral domain. Assuming a Gaussian distribution, the FEL spectral bandwidth during the data acquisition in the glycine experiment can be calculated to be 1.24 eV (FWHM) or about 0.45% of the central photon energy. We note that this number still includes the instrument functions of the OPIS spectrometers as well as a broadening by the finite size beam profile and pointing jitter of the FEL and is therefore an upper limit.

Data analysis and fitting. In Fig. 1A of the main manuscript each spectrum was normalized by the respective number of detected electrons to account for any fluctuations in FEL pulse energy and other FEL parameters. The single spectra for each wavelength were measured for about 5 to 6 minutes. The average FEL wavelength per bunch train drifted less than 0.1% around the central wavelengths. Each spectrum shown in Fig. 1A is stacked vertically with its offset corresponding to the photon energy set by the undulator gap.

Instead of using the Jacobi transformation for the electron TOF to kinetic energy conversion, the equidistant TOF bins were resampled to equidistant energy bins with a linear filter to avoid aliasing effects. The energy bin size of 0.3 eV was chosen to match the energy width of the first time-of-flight bin in the spectra shown in Fig. 1A.

In Fig. 2A the electron spectra were divided by the total number of detected electrons for each delay to account for any FEL fluctuations and afterwards the background was subtracted. Here, the measurement time was 10 minutes per delay. The y-axis shows the relative change of the electron yield compared to the average yield in percent. All four oscillations were fitted with a sinusoidal curve of the form:

$$f_i(\Delta t) = a_i \cdot \sin(\omega_i \cdot \Delta t + \varphi_i), \quad (3)$$

where a_i is the amplitude, φ_i a phase offset, $\omega_i = \frac{2\pi}{T_i}$ and T_i the period of the oscillation for $i \in [1, 4]$. As the average spectrum over all delays was subtracted for every single delay the resulting relative change of the electron yield in percent naturally oscillates around 0.

The oscillation amplitudes, periods, phases and the goodness R_i^2 of the fits are summarized in Table 1.

For Fig. 2C the kinetic energy range of 224 to 264 eV was split into overlapping intervals with 4 eV width in steps of 1 eV. Each of these delay dependent electron spectra were fitted according to the formula used for Fig. 2A. The result of the 37 individual fits is plotted in Fig. 2C with the central energy of the 4-eV energy range on the y-axis.

All of the kinetic energy ranges from Fig. 2C were also fitted with sinusoidal curves of the same period but free phase and amplitudes according to:

$$f_i(\Delta t) = a_i \cdot \sin(\omega \cdot \Delta t + \varphi_i), \quad (4)$$

where a_i is the amplitude and φ_i a phase offset for $i \in [1, 37]$, $\omega = \frac{2\pi}{T}$ and T the period of the oscillation.

The resulting period T of this fit is indicated in Fig. 2A and Fig. 2E as black dashed lines. The shown error values are the mean of the upper and lower 95% for the 37 individual sinusoidal fits of overlapping energy intervals.

The fitted period presented in this article within two standard deviations, $T = (19.6^{+2.2}_{-1.4})$ fs, corresponds to an energy level separation of the two cationic eigenstates Ψ_α and Ψ_β of $\Delta E \approx (0.21 \pm 0.02)$ eV according to equation (2).

The coincidence event map in Fig. 4 is obtained as follows: Every single-shot kinetic energy spectrum with two electrons is represented by a row vector $S(E_1, \dots, E_N)$, where $1 \dots N$ are the indices of energy bins. It is transformed into an $N \times N$ matrix $M = S^T S$. Then all these single-shot matrices, which are symmetric with respect to the diagonal, are summed up and the diagonal line together with the upper triangle are removed for clarity. Columns and rows of the resulting matrix represent the energies of the first electron and the second electron, respectively. The values of elements p_{mn} of the matrix contain the number of double events, where the first electron had the kinetic energy E_n and the second electron had the kinetic energy E_m .

References

1. F. Calegari, D. Ayuso, A. Trabattoni, L. Belshaw, S. De Camillis, S. Anumula, F. Frassetto, L. Poletto, A. Palacios, P. Decleva, J. B. Greenwood, F. Martín, M. Nisoli, Ultrafast electron dynamics in phenylalanine initiated by attosecond pulses. *Science* **346**, 336 (2014).
2. L. S. Cederbaum, J. Zobeley, Ultrafast charge migration by electron correlation. *Chem. Phys. Lett.* **307**, 205 (1999).
3. C. Arnold, O. Vendrell, R. Santra, Electronic decoherence following photoionization: Full quantum-dynamical treatment of the influence of nuclear motion. *Phys. Rev. A* **95**, 033425 (2017).
4. M. Lara-Astiaso, M. Galli, A. Trabattoni, A. Palacios, D. Ayuso, F. Frassetto, L. Poletto, S. De Camillis, J. Greenwood, P. Decleva, I. Tavernelli, F. Calegari, M. Nisoli, F. Martín, Attosecond pump–probe spectroscopy of charge dynamics in tryptophan. *J. Phys. Chem. Lett.* **9**, 4570 (2018).
5. V. Despré, A. Marciniak, V. Loriot, M. C. E. Galbraith, A. Rouzée, M. J. J. Vrakking, F. Lépine, A. I. Kuleff, Attosecond hole migration in benzene molecules surviving nuclear motion. *J. Phys. Chem. Lett.* **6**, 426 (2015).
6. M. Lara-Astiaso, A. Palacios, P. Decleva, I. Tavernelli, F. Martín, Role of electron–nuclear coupled dynamics on charge migration induced by attosecond pulses in glycine. *Chem. Phys. Lett.* **683**, 357 (2017).
7. M. Vacher, M. J. Bearpark, M. A. Robb, J. P. Malhado, Electron dynamics upon ionization of polyatomic molecules: coupling to quantum nuclear motion and decoherence. *Phys. Rev. Lett.* **118**, 083001 (2017).
8. A. Sanchez-Gonzalez, , T. R. Barillot, R. J. Squibb, P. Kolorenč, M. Agaker, V. Averbukh, M. J. Bearpark, C. Bostedt, J. D. Bozek, S. Bruce, S. Carron Montero, R. N.

Coffee, B. Cooper, J. P. Cryan, M. Dong, J. H. D. Eland, L. Fang, H. Fukuzawa, M. Guehr, M. Ilchen, A. S. Johnsson, C. Liekhus-S, A. Marinelli, T. Maxwell, K. Motomura, M. Mucke, A. Natan, T. Osipov, C. Östlin, M. Pernpointner, V. S. Petrovic, M. A. Robb, C. Sathe, E. R. Simpson, J. G. Underwood, M. Vacher, D. J. Walke, T. J. A. Wolf, V. Zhaunerchyk, J.-E. Rubensson, N. Berrah, P. H. Bucksbaum, K. Ueda, R. Feifel, L. J. Frasinski, J. P. Marangos, Auger electron and photoabsorption spectra of glycine in the vicinity of the oxygen K-edge measured with an X-FEL. *J. Phys. B* **48**, 234004 (2015).

9. D. Ayuso, A. Palacios, P. Decleva, F. Martín, Ultrafast charge dynamics in glycine induced by attosecond pulses. *Phys. Chem. Chem. Phys.* **19**, 19767 (2017).

10. O. Plekan, V. Feyer, R. Richter, M. Coreno, M. de Simone, K. C. Prince, V. Carravetta, Investigation of the amino acids glycine, proline, and methionine by photoemission spectroscopy. *J. Phys. Chem. A* **111**, 10998 (2007).

11. S. Usenko, A. Przystawik, M. A. Jakob, L. L. Lazzarino, G. Brenner, S. Toleikis, Ch. Haunhorst, D. Kip, T. Laarmann, Attosecond interferometry with self-amplified spontaneous emission of a free-electron laser. *Nature Commun.* **8**, 15626 (2017).

12. S. Usenko, A. Przystawik, L. L. Lazzarino, M. A. Jakob, F. Jacobs, C. Becker, C. Haunhorst, D. Kip, T. Laarmann, Split-and-delay unit for FEL interferometry in the XUV spectral range. *Appl. Sci.* **7**, 544 (2017).

13. B. Faatz, E. Plönjes, S. Ackermann, A. Agababyan, V. Asgekar, V. Ayvazyan, S. Baark, N. Baboi, V. Balandin, N. von Bargen, Y. Bican, O. Bilani, J. Bödewadt, M. Böhnert, R. Böspflug, S. Bonfigt, H. Bolz, F. Borges, O. Borkenhagen, M. Brachmanski, M. Braune, A. Brinkmann, O. Brovko, T. Bruns, P. Castro, J. Chen, M. K. Czwalinna, H. Damker, W. Decking, M. Degenhardt, A. Delfs, T. Delfs, H. Deng, M. Dressel, H.-T. Duhme, S. Düsterer, H. Eckoldt, A. Eislage, M. Felber, J. Feldhaus, P. Gessler, M. Gibau, N. Golubeva, T. Golz, J. Gonschior, A. Grebentsov, M. Grecki, C. Grün, S. Grunewald, K. Hacker, L. Hänisch, A. Hage, T. Hans, E. Hass, A. Hauberg, O. Hensler, M. Hesse, K.

Heuck, A. Hidvegi, M. Holz, K. Honkavaara, H. Höppner, A. Ignatenko, J. Jäger, U. Jastrow, R. Kammering, S. Karstensen, A. Kaukher, H. Kay, B. Keil, K. Klose, V. Kocharyan, M. Köpke, M. Körfer, W. Kook, B. Krause, O. Krebs, S. Kreis, F. Krivan, J. Kuhlmann, M. Kuhlmann, G. Kube, T. Laarmann, C. Lechner, S. Lederer, A. Leuschner, D. Liebertz, J. Liebing, A. Liedtke, L. Lilje, T. Limberg, D. Lipka, B. Liu, B. Lorbeer, K. Ludwig, H. Mahn, G. Marinkovic, C. Martens, F. Marutzky, M. Masloev, D. Meissner, N. Mildner, V. Miltchev, S. Molnar, D. Mross, F. Müller, R. Neumann, P. Neumann, D. Nölle, F. Obier, M. Pelzer, H.-B. Peters, K. Petersen, A. Petrosyan, G. Petrosyan, L. Petrosyan, V. Petrosyan, A. Petrov, S. Pfeiffer, A. Piotrowski, Z. Pisarov, T. Plath, P. Pototzki, M. J. Prandolini, J. Prenting, G. Priebe, B. Racky, T. Ramm, K. Rehlich, R. Riedel, M. Roggli, M. Röhling, J. Rönsch-Schulenburg, J. Rossbach, V. Rybnikov, J. Schäfer, J. Schaffran, H. Schlarb, G. Schlesselmann, M. Schlösser, P. Schmid, C. Schmidt, F. Schmidt-Föhre, M. Schmitz, E. Schneidmiller, A. Schöps, M. Scholz, S. Schreiber, K. Schütt, U. Schütz, H. Schulte-Schrepping, M. Schulz, A. Shabunov, P. Smirnov, E. Sombrowski, A. Sorokin, B. Sparr, J. Spengler, M. Staack, M. Stadler, C. Stechmann, B. Steffen, N. Stojanovic, V. Sychev, E. Syresin, T. Tanikawa, F. Tavella, N. Tesch, K. Tiedtke, M. Tischer, R. Treusch, S. Tripathi, P. Vagin, P. Vetrov, S. Vilcins, M. Vogt, A. de Zubiaurre Wagner, T. Wamsat, H. Weddig, G. Weichert, H. Weigelt, N. Wentowski, C. Wiebers, T. Wilksen, A. Willner, K. Wittenburg, T. Wohlenberg, J. Wortmann, W. Wurth, M. Yurkov, I. Zagorodnov, J. Zemella, Simultaneous operation of two soft x-ray free-electron lasers driven by one linear accelerator. *New J. Phys.* **18**, 062002 (2016).

14. A. I. Kuleff, J. Breidbach, L. S. Cederbaum, Multielectron wave-packet propagation: general theory and application. *J. Chem. Phys.* **123**, 044111 (2005).

15. R. Bonifacio, L. DeSalvo, P. Pierini, N. Piovella, C. Pellegrini, Spectrum, temporal structure, and fluctuations in a high-gain free-electron laser starting from noise. *Phys. Rev. Lett.* **73**, 70 (1994).

16. E. L. Saldin, E. A. Schneidmiller, M. V. Yurkov, The physics of free-electron lasers. (Springer-Verlag, Berlin, 1999).
17. B. Cooper, P. Kolorenč, L. J. Frasinski, V. Averbukh, J. P. Marangos, Analysis of a measurement scheme for ultrafast hole dynamics by few femtosecond resolution x-ray pump–probe Auger spectroscopy. *Faraday Discuss.* **171**, 93 (2014).
18. B. Cooper, V. Averbukh, Single-photon laser-enabled Auger spectroscopy for measuring attosecond electron-hole dynamics. *Phys. Rev. Lett.* **111**, 083004 (2013).
19. A. I. Kuleff, J. Breidbach, L. S. Cederbaum, Charge migration in different conformers of glycine: The role of nuclear geometry. *Chem. Phys.* **338**, 320 (2007).
20. T. Barillot, O. Alexander, B. Cooper, T. Driver, D. Garratt, S. Li, A. Al Haddad, A. Sanchez-Gonzalez, M. Agåker, C. Arrell, M. Bearpark, N. Berrah, C. Bostedt, J. Bozek, C. Brahms, P. H. Bucksbaum, A. Clark, G. Doumy, R. Feifel, L. J. Frasinski, S. Jarosch, A. S. Johnson, L. Kjellsson, P. Kolorenč, Y. Kumagai, E. W. Larsen, P. Matia-Hernando, M. Robb, J.-E. Rubensson, M. Ruberti, C. Sathe, R. J. Squibb, A. Tan, J. W. G. Tisch, M. Vacher, D. J. Walke, T. J. A. Wolf, D. Wood, V. Zhaunerchyk, P. Walter, T. Osipov, A. Marinelli, T. Maxwell, R. Coffee, A. A. Lutman, V. Averbukh, K. Ueda, J. P. Cryan, J. P. Marangos, Correlation Driven Transient Hole Dynamics Resolved in Space and Time in the Isopropanol Molecule. *arXiv:2105.06507 [physics.chem-ph]*
21. M. Ruberti, Restricted correlation space B-spline ADC approach to molecular ionization: theory and applications to total photoionization cross-sections. *J. Chem. Theory Comput.* **15**, 3635 (2019).
22. M. Ruberti, Onset of ionic coherence and ultrafast charge dynamics in attosecond molecular ionisation. *Phys. Chem. Chem. Phys.* **21**, 17584 (2019).
23. M. Ruberti, Quantum electronic coherences by attosecond transient absorption spectroscopy: ab initio B-spline RCS-ADC study. *Faraday Discussions*, 2020, DOI: 10.1039/D0FD00104J.

24. P. Kolorenč, V. Averbukh, Fano-ADC(2,2) method for electronic decay rates. *J. Chem. Phys.* **152**, 214107 (2020).
25. D. Toffoli, M. Stener, G. Fronzoni, P. Decleva, Convergence of the multicenter B-spline DFT approach for the continuum. *Chem. Phys.* **276**, 25 (2002).
26. J. J. Neville, Y. Zheng, C. E. Brion, Glycine valence orbital electron densities: comparison of electron momentum spectroscopy experiments with Hartree-Fock and density functional theories. *J. Am. Chem. Soc.* **118**, 10533 (1996).
27. H.-J. Werner, P. J. Knowles, G. Knizia, F. R. Manby, M. Schutz, Molpro: a general-purpose quantum chemistry program package. *WIREs Comput. Mol. Sci.* **2**, 242 (2012).
28. Y. Zhang, J. D. Biggs, W. Hua, K. E. Dorfman, S. Mukamel, Three-Dimensional Attosecond Resonant Stimulated X-Ray Raman Spectroscopy of Electronic Excitations in Core-ionized Glycine. *Phys. Chem. Chem. Phys.* **16**, 24323 (2014).
29. M. Kowalewski, K. Bennett, K. E. Dorfman, S. Mukamel, Catching Conical Intersections in the Act: Monitoring Transient Electronic Coherences by Attosecond Stimulated X-Ray Raman Signals. *Phys. Rev. Lett.* **115**, 193003 (2015).
30. D. Keefer, T. Schnappinger, R. de Vivie-Riedle, S. Mukamel, Visualizing conical intersection passages via vibronic coherence maps generated by stimulated ultrafast X-ray Raman signals. *Proc. Natl. Acad. Sci.* **117**, 24069 (2020).
31. D. Keefer, V. M. Freixas, H. Song, S. Tretiak, S. Fernandez-Alberti, S. Mukamel, Monitoring molecular vibronic coherences in a bichromophoric molecule by ultrafast X-ray spectroscopy. *Chem. Sci.* **12**, 5286 (2021).
32. P. M. Kraus, B. Mignolet, D. Baykusheva, A. Rupenyan, L. Horný, E. F. Penka, G. Grassi, O. I. Tolstikhin, J. Schneider, F. Jensen, L. B. Madsen, A. D. Bandrauk, F. Remacle, H. J. Wörner, Measurement and laser control of attosecond charge migration in ionized iodoacetylene. *Science* **350**, 790 (2015).

Acknowledgements

General: We thank the late Prof. Dr. Wilfried Wurth for many inspiring discussions.

Funding: This work was funded by the Deutsche Forschungsgemeinschaft (DFG, German Research Foundation) through the Cluster of Excellence ‘Advanced Imaging of Matter’ (EXC 2056 - project ID 390715994), the collaborative research center ‘Light-induced Dynamics and Control of Correlated Quantum Systems’ (SFB-925 – project 170620586), the projects KI 482/20-1 and LA 1431/5-1, and by the Federal Ministry of Education and Research of Germany under Contract No. 05K10CHB.

Author contributions: T.L. led the project. D.S., S.U. and A.P. prepared the endstation. S.Dei. and J.V. developed the magnetic-bottle electron spectrometer. J.R.S. and M.K.C. prepared the FEL. M.K., S.Due, S.T., S.P., I.B., M.M. and M.B. prepared the photon beamline and ran the online photon diagnostics. S.U., A.P., C.H. and D.K. developed the split-and-delay unit coated with nickel by L.B. and R.R. The experiment was performed by D.S., S.U., A.P., K.M., S.Dei., A.H., G.H., P.S. and T.L. The data were analyzed by D.S and S.U. with support from P.S., G.H. and A.K. The results were interpreted by D.S., S.U., A.P. and T.L. Theory and modelling were performed by M.R. and P.K. with support from V.A. and J.P.M. The corresponding sections in the supplementary information were written by M.R. The manuscript was written by T.L with contributions from D.S., S.U., and A.P., as well as input from all authors.

Competing interests: The authors declare no competing financial interests.

Data and materials availability: The authors declare that the main data supporting the findings of this study are available within the article and its supplementary information file. Extra data are available from the corresponding author upon reasonable request.

Figures and Tables

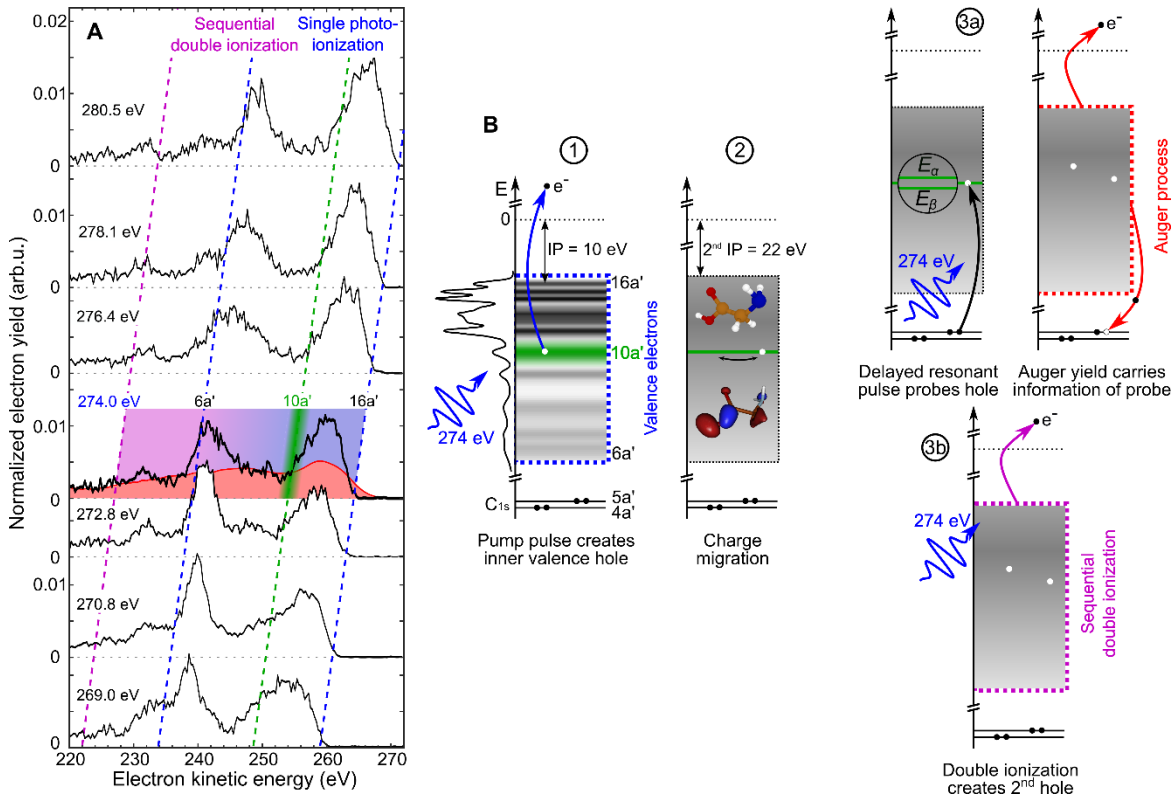


Fig. 1. X-ray photoelectron spectroscopy of glycine. (A) Kinetic energy distributions of detected electrons as a function of FEL photon energy using single pulses, i.e. $\Delta t = 0$. Tilted lines (dashed blue, dashed violet) mark the energy ranges of single photoionization and sequential double photoionization of valence and inner-valence electron orbitals (6a' - 16a', 1a'' - 4a''), respectively. An experimental Auger electron spectrum (red) for C1s core vacancies (4a', 5a') is reproduced from ref. (8). The spectral bandwidth of the ionizing radiation in the vicinity of the 10a' molecular orbital is indicated (green). (B) A single-color pump-probe scheme is applied to track charge dynamics initiated by photoelectron emission from the 10a' molecular orbital. The total cascade involves several different processes: (1) photoionization, (2) charge migration triggered by the beating of the quantum interference, (3a) resonant carbon 1s core hole excitation and Auger decay, as well as (3b) sequential double photoionization of valence

electrons. The individual steps are depicted as a sequence of energy diagrams. The density of states is indicated by using the experimental data reproduced from ref. (10).

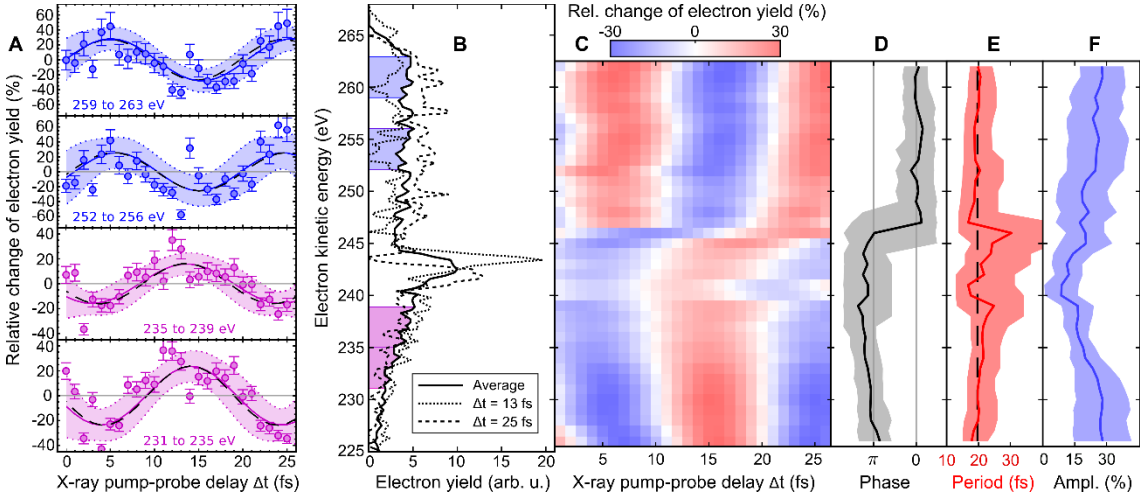


Fig. 2. Phase-sensitive electron wave packet interferometry of glycine with 274 eV photons. **(A)** Relative change of the detected electron yield in kinetic energy ranges with contributions from Auger emission superimposed with sequential double ionization as a function of x-ray pump-probe delay. The solid lines are the sinusoidal fitting functions of time period T . The 95% confidence bounds are given by dotted lines. **(B)** Kinetic energy distributions of detected electrons recorded for pump-probe delays $\Delta t = 13$ fs and $\Delta t = 25$ fs compared with the average electron spectrum over all delays. **(C)** Delay dependent electron spectra fitted in steps of 1 eV with sinusoidal functions and 4 eV detection range having the oscillation period, amplitude and phase of the quantum beat as free parameters. The fitting functions are presented as a false color plot. **(D)** Phases, **(E)** periods and **(F)** amplitudes of the sinusoidal functions (solid black, solid red and solid blue line) depending on the kinetic energy of detected electrons. The 95% confidence bounds are given by the shaded areas. The black dashed lines

shown in (A) and (E) are the result of using a single time period $T = (19.6^{+2.2}_{-1.4})$ fs for fitting the complete data set.

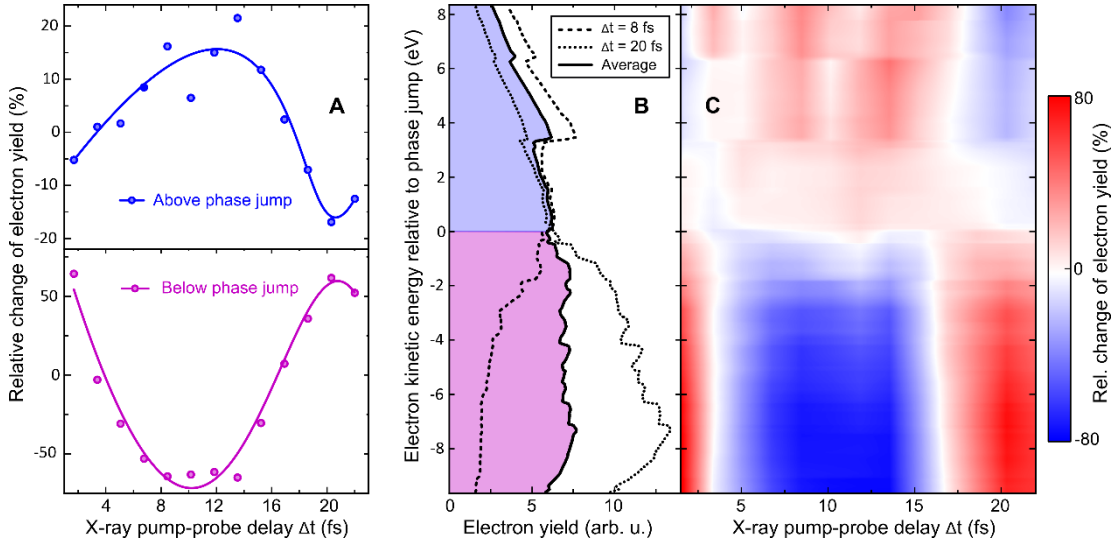


Fig. 3. *Ab-initio* TD B-spline RCS-ADC simulation of experimental observables using the measured FLASH pulse parameters. (A) Relative change of the detected electron yield in kinetic energy ranges above and below the phase jump including contributions from Auger emission and sequential double ionization as a function of x-ray pump-probe delay. The solid lines are guide-to-the eye showing the onset of an oscillatory behavior with a time period of ~ 20 fs. (B) Kinetic energy distributions of emitted electrons simulated for pump-probe delays $\Delta t = 8$ fs and $\Delta t = 20$ fs compared with the average electron spectrum over all calculated delays. (C) Delay dependent electron spectra presented as a false color plot system (for details see supplementary information).

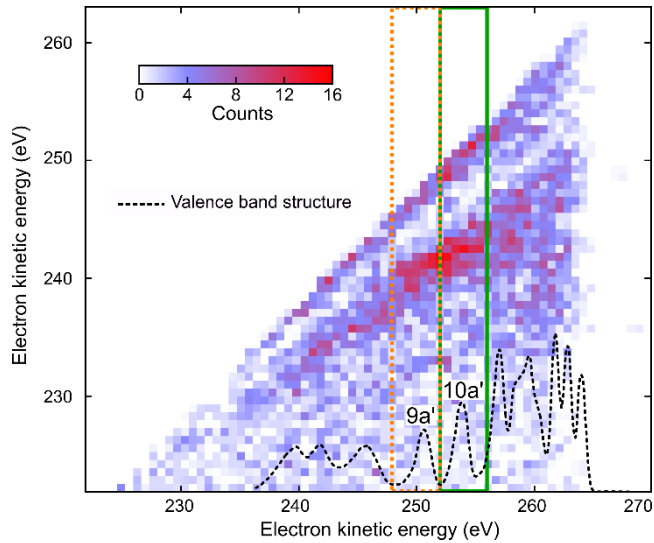


Fig. 4. Two-electron coincidence spectroscopy of glycine with 274 eV photons. Coincidence map of two-electron detection. Photoelectron (10a', 9a') – Auger electron coincidences following the resonant x-ray transition ($1s \rightarrow 1h$) are indicated (green and orange squares). The density of valence states is indicated (dotted black) by using the experimental data reproduced from ref. (10). Valence electron emission from x-ray probe-induced sequential double ionization contributes to an uncorrelated background with respect to the (initial) x-ray pump-induced photoionization events, which allows observing the fingerprint of the resonant Auger decay.

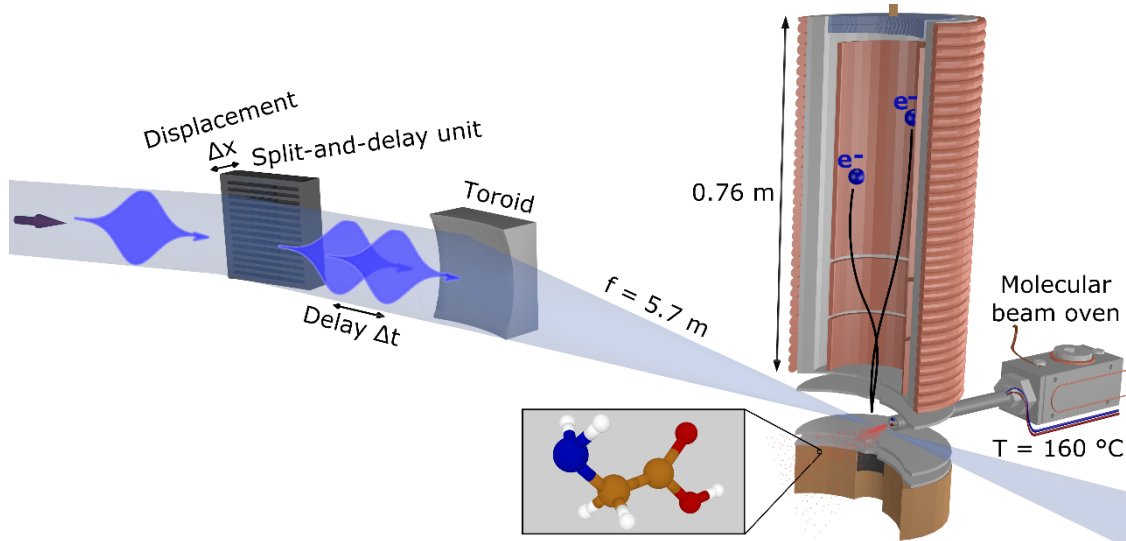


Fig. 5. Schematic setup. Experimental setup for the pump-probe measurements of glycine at FLASH2.

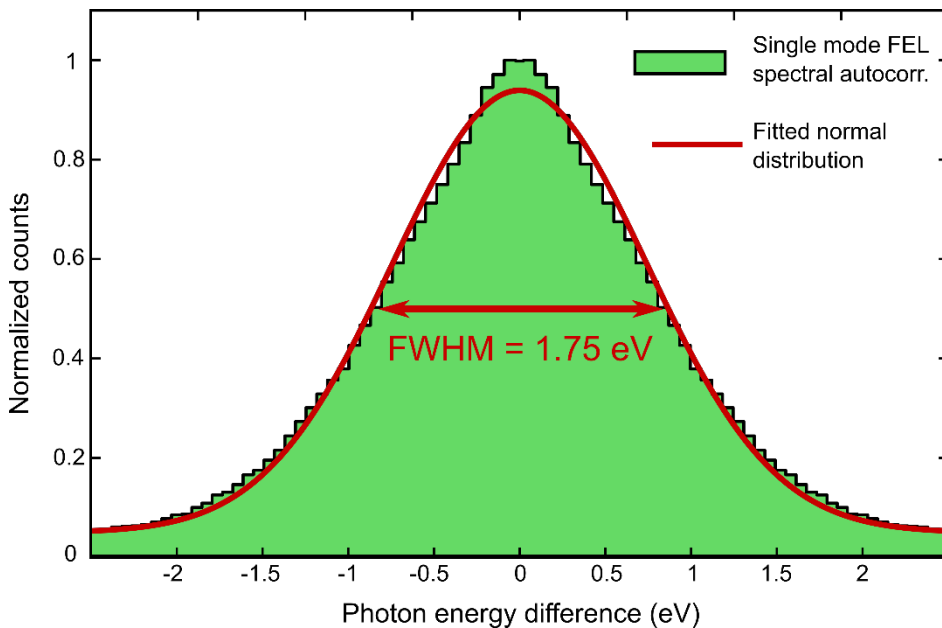


Fig. 6. FEL photon energy autocorrelation for the dataset shown in Fig. 2. Photoionization from the Argon $2p_{1/2}$ and $2p_{3/2}$ orbitals was used to infer the FEL photon energy from four TOF spectrometers.

Table 1. Fitting parameters of sinusoidal curves of form of equation (3). The oscillation amplitudes, periods, phases and the goodness R_i^2 of the fits describing the experimental data shown in Fig. 2A are summarized.

energy range	amplitude	period	phase	goodness
259 to 263 eV	$a_1 \approx (28 \pm 11)\%$	$T_1 \approx (20.6^{+3.8}_{-2.8})$ fs	$\varphi_1 \approx (0.0 \pm 0.2)\pi$	$R_1^2 \approx 0.58$
252 to 256 eV	$a_2 \approx (26 \pm 14)\%$	$T_2 \approx (18.8^{+5.4}_{-3.4})$ fs	$\varphi_2 \approx (-0.1 \pm 0.3)\pi$	$R_2^2 \approx 0.37$
235 to 239 eV	$a_3 \approx (16 \pm 6)\%$	$T_3 \approx (21.4^{+6.2}_{-3.9})$ fs	$\varphi_3 \approx (1.2 \pm 0.3)\pi$	$R_3^2 \approx 0.55$
231 to 235 eV	$a_4 \approx (24 \pm 9)\%$	$T_4 \approx (20.5^{+4.6}_{-3.2})$ fs	$\varphi_4 \approx (1.1 \pm 0.3)\pi$	$R_4^2 \approx 0.58$

Supplementary Materials for

Electronic Quantum Coherence in Glycine Molecules

Probed with Ultrashort X-ray Pulses in Real Time

David Schwickert, Marco Ruberti*, Přemysl Kolorenč, Sergey Usenko, Andreas Przystawik, Karolin Baev, Ivan Baev, Markus Braune, Lars Bocklage, Marie Kristin Czwalinna, Sascha Deinert, Stefan Düsterer, Andreas Hans, Gregor Hartmann, Christian Haunhorst, Marion Kuhlmann, Steffen Palutke, Ralf Röhlsberger, Juliane Rönsch-Schulenburg, Philipp Schmidt, Sven Toleikis, Jens Viefhaus, Michael Martins, André Knie, Detlef Kip, Vitali Averbukh, Jon P. Marangos, Tim Laarmann*

**Corresponding author. Email: m.ruberti11@imperial.ac.uk; tim.laarmann@desy.de*

This PDF file includes:

Supplementary Text
Figs. S1 to S5

Supplementary Text

S1. Theoretical methods.

Advanced theoretical modelling and simulation of the photoionization dynamics of the glycine molecule triggered by the x-ray pump and probe laser pulses is performed here, from first-principles, within the framework of the cutting-edge time-dependent B-spline restricted correlation space (RCS) – algebraic diagrammatic construction (ADC) *ab initio* methods (21-23). Both interactions of the neutral glycine molecule and its cation with the pump and probe x-ray femtosecond pulses, respectively, are described from first-principles. The simulations of photoionization during the pump and probe steps are carried out, within the frozen-nuclei approximation, at the equilibrium geometry of the Gly I conformer. We also analyse the effect of the geometry-spread of the ground state nuclear wavefunction on the survival of the quantum electronic coherences in the 10a' and 9a' ionized bands (see Section S3).

S1.1 First ionization of the neutral species by the x-ray pump pulse.

Within B-spline RCS-ADC, the single-electron orbitals are expanded in a multicenter B-spline basis set (21, 25), designed to accurately describe both bound and ionized states of the neutral molecule. The resulting Hilbert space of Hartree-Fock (HF) virtual orbitals (ϕ_α), is subsequently partitioned into two orthonormal subspaces: the restricted correlation space (RCS) (χ_α), designed to accurately describe the localised short-range correlation of the system, and its orthonormal complement, the ionization space (IS) (ψ_μ), which describes the long-range part of the photoelectron wavefunction and complements the RCS in order to represent the electronic wavefunction over the entire spatial region (21). Here and in what follows, the α, β, \dots and μ, ν, \dots indices refer to the virtual space (unoccupied) RCS and IS orbitals, respectively, whereas i, j, k, \dots , indicate the occupied HF molecular orbitals.

Within the time-dependent (TD) B-spline RCS-ADC(n) approach to molecular photoionization dynamics (22, 23), the 3D time-dependent Schrödinger equation (TDSE) for an N-electron polyatomic molecule interacting with an ultrashort laser pulse

$$i \hbar \frac{\partial |\Psi^N(t)\rangle}{\partial t} = \hat{H}_{Pump}^N(t) |\Psi^N(t)\rangle \quad (1)$$

is solved by expanding the TD many-electron wavefunction in the basis of the ground and excited RCS-ADC(n) states (22, 23)

$$|\Psi^N(t)\rangle = \sum_{m,\mu} c_{m,\mu}(t) \hat{a}_\mu^\dagger |\Phi_m^{N-1,RCS}\rangle + \sum_{I_{RCS}} c_{I_{RCS}}(t) |\tilde{\Psi}_{I_{RCS}}^N\rangle^{[n]} + c_0(t) |\Psi_0^{RCS}\rangle^{[n]}. \quad (2)$$

Here $|\Psi_0^{RCS}\rangle^{[n]}$ is the n-th order RCS correlated ground state, and $|\tilde{\Psi}_{I_{RCS}}^N\rangle^{[n]}$ indicates the excited intermediate states of the nth-order ADC(n) scheme, built using the single-particle RCS basis. The ansatz of Eq. (2) includes a full description of electron correlation effects, such as shakeup processes, breakdown of the molecular orbital (MO) picture and inter-channel couplings in the continuum, which can play an essential role both during the ionization event and the post-ionization charge dynamics.

Within the extended second-order ADC(2)x scheme for many-electron excitation used in this work, the excited (N)-electron intermediate states span the configuration space consisting of one-hole – one-particle (1h1p) ($|\tilde{\Psi}_{\alpha i}^N\rangle^{[n]}$) and two-hole – two-particle (2h2p) ($|\tilde{\Psi}_{\alpha\beta ij}^N\rangle^{[n]}$) excitation classes built on top of the RCS correlated ground state (21). The first term on the right-hand side of Eq. (2) describes the IS configuration states of B-spline RCS-ADC, which take the form of ionization-channel-specific product-states and reads $|\Psi_{\mu,m}^N\rangle = \hat{a}_\mu^\dagger |\Phi_m^{N-1,RCS}\rangle$, where \hat{a}_μ^\dagger is the creation operator of an electron in the IS molecular orbital $\psi_\mu(r)$, and $|\Phi_m^{N-1,RCS}\rangle$ denotes the RCS-ADC ionic eigenstates. In this work, the latter have been calculated using the ADC(2,2) (24) method for (N-1)-electron systems.

Thus, the $|\Phi_m^{N-1,RCS}\rangle$ are obtained by diagonalizing the ionic Hamiltonian calculated at the ADC(2,2) level of theory and using the single-particle RCS basis set

$$\hat{H}_{ADC(2,2)}^{N-1,RCS} |\Phi_m^{N-1,RCS}\rangle = I_m^p |\Phi_m^{N-1,RCS}\rangle, \quad (3)$$

where the ionization energy is given by $I_m^p = E_m^{N-1} - E_0^{RCS}$ and E_0^{RCS} is the energy of the RCS ground state. Within the RCS-ADC(2,2) scheme, the contributions to electron correlation of one-hole (1h) and two-hole – one-particle (2h1p) configurations, is taken into account in a better-balanced way compared to both ADC(2)x and ADC(3) methods (24), making the approach more appropriate for spectral region with strong MO picture breakdown. The ionic states are expanded into 1h, 2h1p and 3h2p configurations derived from the correlated RCS ground state of the neutral molecule

$$|\Phi_m^{N-1,RCS}\rangle = \sum_i V_{i,m}^+ |\tilde{\Phi}_i^{N-1}\rangle + \sum_{\alpha ij} V_{\alpha ij,m}^+ |\tilde{\Phi}_{\alpha ij}^{N-1}\rangle + \sum_{\alpha\beta ijk} V_{\alpha\beta ijk,m}^+ |\tilde{\Phi}_{\alpha\beta ijk}^{N-1}\rangle. \quad (4)$$

The total time-dependent Hamiltonian of Eq. (1) reads

$$\hat{H}_{Pump}^N(t) = \hat{H}_{RCS-ADC}^N + \hat{D}_{RCS-ADC}^N E_{Pump}(t) - i\hat{W}, \quad (5)$$

where a complex absorbing potential (CAP) of the form $\hat{W} = \eta(r - r_{CAP})^2$ ($r \geq r_{CAP}$) is used to eliminate wave packet reflections from the boundaries of the B-spline radial grid. The laser-molecule interaction driven by the x-ray pump electric field ($E_{Pump}(t)$) is described within the dipole approximation in the length form, and $\hat{H}_{RCS-ADC}^N$ and $\hat{D}_{RCS-ADC}^N$ are the representation of the shifted field-free Hamiltonian $\hat{H} = \hat{H} - E_0^{RCS}$ and the dipole operator \hat{D} , respectively, in the space of RCS-ADC intermediate states (see Eq. (2)). These matrices contain as sub-blocks the conventional ADC matrices computed within the RCS-based excitation space, and are further augmented with the blocks corresponding to the product-states, which describe ionization and interaction in the continuum (21-23). All the blocks of the $\hat{H}_{RCS-ADC}^N$ matrix are evaluated at the ADC(2)x level of theory, with the only exception of the Hamiltonian terms describing the energy of the (N-1)-electron ionic states, evaluated at the ADC(2,2) level of theory.

The time propagation of the unknown coefficients of the neutral many-electron wavefunction Eq. (2) is performed by means of the Arnoldi/Lanczos algorithm (22, 23). During the simulation of the pump step, we have included into the expansion of the many-electron

wavefunction only the open ionization channels with energy up to the double ionization threshold (DIP) and characterized by an (ionization) spectral intensity value (see ref. (21, 22)) greater than 1%. These states will be denoted in the following as $|\Phi_{n,\text{Pump-ionized}}^{N-1,RCS}\rangle$. Doing so guarantees that all the ionic states that can be effectively populated in the x-ray pump ionization, and consequently play the main role in the ensuing many-electron dynamics taking place in the molecular cation, are accounted for (22, 23). The contribution of ionic states with a smaller spectral-intensity value, as well as of deeper core-ionization channels, was indeed found to be negligible.

The pump-triggered coherent electron dynamics is obtained by calculating, in the basis of ionic eigenstates $|\Phi_{m,\text{Pump-ionised}}^{N-1,RCS}\rangle$, the time-dependent reduced ionic density matrix (R-IDM) $\hat{\rho}^{R-IDM}(t)$ of the molecular ion emerging from the femtosecond pump-ionization step. This is achieved by tracing out the unobserved photoelectron degree of freedom from the total time-dependent density matrix of the N-electron system

$$\hat{\rho}^{R-IDM}(t) = \text{Tr}_\mu [|\Psi^N(t)\rangle\langle\Psi^N(t)|]. \quad (6)$$

Doing so, and using the many-electron states of Eq. (2) within the TD RCS-ADC(n) framework, yields in the basis of ADC(2,2) ionic eigenstates

$$\begin{aligned} \hat{\rho}_{m,n}^{R-IDM}(t) = & \sum_{\mu} c_{m\mu}(t) [c_{n\mu}(t)]^* \\ & + 2e^{i(l_n^p - l_m^p)t} \int_{-\infty}^t \sum_{\mu,\nu} w_{\nu,\mu} c_{m\mu}(t') [c_{n\nu}(t')]^* e^{-i(l_n^p - l_m^p)t'} dt', \end{aligned} \quad (7)$$

where the latter term corrects for the loss of norm introduced by the CAP (21), l_m^p is the ionization potential of the ionic state m and $w_{\nu,\mu}$ is the CAP matrix element between photoelectron IS orbitals μ and ν . From now on we shall omit the R-IDM superscript and denote the reduced ionic density matrix as $\rho_{m,n}$.

The R-IDM fully describes the mixed ionic state prepared by attosecond molecular ionization: the TD population of the different ionic eigenstates is given by the diagonal elements

$$p_n(t) = |\rho_{n,n}(t)|. \quad (8)$$

while the off-diagonal ones $\rho_{m,n}$ are related to the degrees of quantum electronic coherence, $0 \leq G_{m,n} \leq 1$, between any pair of populated ionic channels m and n

$$G_{m,n}(t) = \frac{|\rho_{m,n}(t)|}{\sqrt{p_m(t) * p_n(t)}}. \quad (9)$$

In addition, the relative phases $\varphi_{m,n}$ between the partially-coherently populated eigenstates of energies I_m^p and I_n^p are extracted from the phases of the R-IDM off-diagonal matrix elements and read

$$\varphi_{m,n} = \arg \left[\rho_{m,n}(t) e^{+i(I_m^p - I_n^p)t} \right]. \quad (10)$$

The relative phase matrix is antisymmetric, i.e. $\varphi_{m,n} = -\varphi_{n,m}$, as follows from the hermiticity of the density matrix ($\rho_{n,m} = \rho_{m,n}^*$).

Finally, diagonalization of the ionic density matrix yields the so-called Schmidt decomposition (23). The latter represents a powerful tool to analyze the produced mixed state of the cationic system, allowing one to express it as a fully-incoherent sum of several (N_{ionic}) fully quantum-coherent pure states, each of them populated with weight r_m and represented by the projection operator \hat{P}_m :

$$\hat{\rho}(t) = \sum_{m=1, N_{ionic}} r_m(t) \hat{P}_m(t) = \sum_{m=1, N_{ionic}} r_m(t) |\Phi_m^\rho(t)\rangle \langle \Phi_m^\rho(t)| \quad (11)$$

This operation is called purification of the density matrix.

S1.2 Second ionization of the cationic species by the x-ray probe pulse.

In this work, we explicitly simulate the interaction of the pump-ionized system with the probe pulse. Doing so allows us to calculate the time-delay dependence of probe-induced electron emission from the pump-ionized glycine cation, thus obtaining a realistic description of the ultrafast electronic observables measured in the experiment.

The formal validity of the presented theoretical framework relies on non-overlapping pump and probe pulses. The reason for this restriction is that, while the current B-spline RCS-ADC implementation can accurately treat many-electron dynamics with one photoelectron in the continuum, it cannot yet afford the modelling of two photoelectrons in the continuum at the same time. The latter, which would in fact be more appropriate in the case of overlapping pump and probe pulses, would also require one to extend the expansion of the many-electron RCS-ADC wavefunction (Eq. (2)) by states of the type $\hat{a}_\mu^\dagger \hat{a}_\nu^\dagger | \Omega_m^{N-2,RCS} \rangle$, thus posing an extra demand on the computation by means of the TD RCS-ADC machinery. However, in practise, this only limits the range pump-probe scenarios that can be numerically tackled to the ones corresponding to time-delays greater than the duration of the x-ray pulses involved $\tau_d > T_{Pump}/2$, i.e. in this case corresponding to delay times of 1.3 fs or longer.

The time-dependent description of the cation-probe interaction is performed by solving the time-dependent von Neumann equations (23) for the characterized reduced ionic density matrix (Eq. (7)) interacting with the probe laser field

$$\frac{d}{dt} \hat{\rho}(t) = -\frac{i}{\hbar} [\hat{H}_{Probe}^{N-1}(t), \hat{\rho}(t)]. \quad (12)$$

Eq. (12) is solved by using the B-spline RCS-ADC method (21-23), which we extended here to describe the photoionization dynamics of (N-1)-electron systems. The solution provides an explicit description of the ionization continua of the dication as well as of the Auger decay process, and both photoemission channels are included in the calculation. In particular, this equation can be solved by taking advantage of the Schmidt decomposition Eq. (11) of the ionic

density matrix upon the pump-ionization step. It allows us to tackle the solution of Eq. (12) by propagating $N_{ionic}^{t=0}$ independent TDSE,

$$i \hbar \frac{\partial |\Phi_m^\rho(t)\rangle}{\partial t} = \hat{H}_{Probe}^{N-1}(t) |\Phi_m^\rho(t)\rangle \quad m = 1, \dots, N_{ionic}^{t=0} \quad (13)$$

corresponding to the individual pure ionic states obtained by the purification of the initial (before the interaction with the probe pulse) ionic density matrix prepared by the pump pulse. The time-dependent $|\Phi_m^\rho(t)\rangle$ states can be expanded in the basis of (N-1)-electron RCS-ADC states as

$$|\Phi_m^{\rho,N-1}(t)\rangle = \sum_{m,\mu} c_{m,\mu}(t) \hat{a}_\mu^\dagger |\Omega_m^{N-2,RCS}\rangle + \sum_{I_{RCS}} c_{I_{RCS}}(t) |\tilde{\Phi}_{I_{RCS}}^{N-1}\rangle^{[n]}. \quad (14)$$

This expression can be further simplified, and renormalized in terms of cationic eigenstates, by expressing the $|\tilde{\Phi}_{I_{RCS}}^{N-1}\rangle$ RCS configurations in terms of the RCS ionic eigenstates $|\Phi_{n',Pump-ionized}^{N-1,RCS}\rangle$ and $|\Phi_{n'',Core}^{N-1,RCS}\rangle$. One derives

$$|\Phi_m^{\rho,N-1}(t)\rangle = \sum_{n,\mu} c_{m;n\mu}(t) \hat{a}_\mu^\dagger |\Omega_n^{N-2,RCS}\rangle + \sum_{n'} c_{m;n'}(t) |\Phi_{n',Pump-ionized}^{N-1,RCS}\rangle + \sum_{n''} c_{m;n''}(t) |\Phi_{n'',Core}^{N-1,RCS}\rangle. \quad (15)$$

In Eq. (15) we have thus expressed the wavefunction of the time-dependent pure-state channel $|\Phi_m^{\rho,N-1}(t)\rangle$ as an expansion over the full electronic spectrum of the ionic subsystem, including both its low-energy bound excitations, i.e. the valence-ionized states populated by the pump pulse, the C(1s) core-ionized states, which were not populated in the pump-step simulation, and the electronic continua of the valence-doubly-ionized states.

The time-dependent ionic Hamiltonian $\hat{H}_{Probe}^{N-1}(t)$ in the dipole approximation is given by

$$\hat{H}_{Probe}^{N-1}(t) = \hat{H}_{RCS-ADC}^{N-1} + \hat{D}_{RCS-ADC}^{N-1} E_{Probe}(t) - i\hat{W}, \quad (16)$$

where $\hat{H}_{RCS-ADC}^{N-1}$ and $\hat{D}_{RCS-ADC}^{N-1}$ are again the representations of the shifted field-free ionic Hamiltonian and the dipole operator, respectively, in the (N-1)-electron configuration space spanned by all the ionic states of Eq. (15). In this work, the RCS core-ionized states are calculated at the ADC(2)x level of theory employing the core-valence approximation, i.e. $\langle \Phi_{n',\text{Pump-ionized}}^{N-1,RCS} | \hat{H}_{RCS-ADC}^{N-1} | \Phi_{n'',\text{Core}}^{N-1,RCS} \rangle = 0$, and read

$$|\Phi_{n'',\text{Core}}^{N-1,RCS}\rangle = I_{n''}^p |\Phi_{n'',\text{Core}}^{N-1,RCS}\rangle ; \quad I_{n''}^p = E_{n''}^{N-1} - E_0^{RCS} \quad (17)$$

$$|\Phi_{n'',\text{Core}}^{N-1,RCS}\rangle = \sum_i V_{i,n''}^+ |\tilde{\Phi}_i^{N-1}\rangle + \sum_{\alpha ij} V_{\alpha ij,n''}^+ |\tilde{\Phi}_{\alpha ij}^{N-1}\rangle. \quad (18)$$

In Eq. (18) each of the ADC configurations in the expansion features at least one hole-index (i, j) correspond to either the 4a' or 5a' C(1s) occupied molecular orbital; Eq. (18) thus describes the core-ionized states of the glycine cation in the energy range of the Carbon K-edge.

The first term on the right-hand side of Eq. (15) describes the IS configuration states of B-spline RCS-ADC for (N-1)-electron systems. These states take the form of ionization-channel-specific product-states

$$|\Phi_{\mu,n}^{N-1}\rangle = \hat{a}_\mu^\dagger |\Omega_n^{N-2,RCS}\rangle \quad (19)$$

built upon the RCS-ADC eigenstates of the dication $|\Omega_n^{N-2,RCS}\rangle$. The latter are obtained by diagonalizing the dicationic ADC Hamiltonian $\hat{H}_{ADC(1)}^{N-2,RCS}$ computed using the single-particle RCS basis set

$$\hat{H}_{ADC(1)}^{N-2,RCS} |\Omega_n^{N-2,RCS}\rangle = DIP_n |\Omega_n^{N-2,RCS}\rangle, \quad (20)$$

where the double-ionization energy is given by $DIP_n = E_n^{N-2} - E_0^{RCS}$. In this work, the eigenstates of the dication (produced by the probe pulse)

$|\Omega_{n,\text{Probe-ionized}}^{N-2,RCS}\rangle = \sum_{ij} V_{ij,n}^{2+} |\tilde{\Omega}_{ij}^{N-2}\rangle$ are described within the ADC(1) scheme for (N-2)-electron systems, and are expanded into 2h $|\tilde{\Omega}_{ij}^{N-2}\rangle$ configurations derived from the correlated ground state of the neutral molecule. They are thus described up to first order in the many-body perturbation theory.

The remaining blocks $\langle \Phi_{n',\text{Pump-ionized}}^{N-1,RCS} | \hat{H}_{RCS-ADC}^{N-1} | \Phi_{\mu,n}^{N-1} \rangle$, $\langle \Phi_{n',\text{Core}}^{N-1,RCS} | \hat{H}_{RCS-ADC}^{N-1} | \Phi_{\mu,n}^{N-1} \rangle$ and $\langle \Phi_{v,n'}^{N-1} | \hat{H}_{RCS-ADC}^{N-1} | \Phi_{\mu,n}^{N-1} \rangle$ are calculated at the ADC(2)x level of theory.

The initial condition for the solution of Eq. (13) reads

$$|\Phi_m^{\rho,N-1}(t = \tau_d)\rangle = \sum_{n'} c_{m;n'}(t = 0) e^{-\frac{i}{\hbar} I_{n'}^p \tau_d} |\Phi_{n',\text{Pump-ionized}}^{N-1,RCS}\rangle. \quad (21)$$

It is important to note that the validity of the presented modelling of the cation-probe interaction requires the effect of the interaction with the x-ray probe pulse, on the ensuing many-electron dynamics of interest, to dominate over the residual interaction of the produced cationic system with the emitted photoelectron. For the aforementioned values of the pump-probe time-delay used here, this is indeed the case, as confirmed by the fact that the ionic density matrix $\hat{\rho}(t)$ stabilizes within the first 300 as after the pump ionization event. This is a result of the high kinetic energy of the photoelectron leaving the molecular region, and justifies the neglect of the pump-emitted photoelectron during the description of the probe step, i.e. at times greater than 1.3 fs.

Analogously to the pump-step procedure, we calculate here the time-dependent reduced dicationic density matrix (R-DIDM) $\hat{\rho}^{R-DIDM}(t)$ emerging from the probe-ionization step, by tracing out the unobserved photoelectron degree of freedom from the total time-dependent density matrix of the (N-1)-electron system

$$\hat{\rho}^{R-DIDM}(t) = \hat{\rho}^{2+} = \text{Tr}_\mu [|\Phi_m^{\rho,N-1}(t)\rangle \langle \Phi_m^{\rho,N-1}(t)|]. \quad (22)$$

The density matrix of the molecular dication, in the basis of ADC(2) dicationic eigenstates $|\Omega_{m, \text{Probe-ionised}}^{N-2, \text{RCS}}\rangle$, reads

$$\hat{\rho}_{m,n}^{2+}(t) = \sum_{\mu} c_{m\mu}(t) [c_{n\mu}(t)]^* + 2e^{i(DIP_n - DIP_m)t} \int_{-\infty}^t \sum_{\mu,\nu} w_{\nu,\mu} c_{m\mu}(t') [c_{n\nu}(t')]^* e^{-i(DIP_n - DIP_m)t'} dt'. \quad (23)$$

Finally, the measurable photoemission spectrum resulting from the interaction of the x-ray probe pulse with the pump-prepared cationic system is recovered by convoluting the discrete, final populations of dicationic states $p_n^{2+}(t) = |\rho_{n,n}^{2+}(t)|$ with a Gaussian function of FWHM width $\delta \approx 2.5 \text{ eV}$

$$p_{e^-}^{\text{Probe-pulse}}(E) = \sum_n p_n^{2+}(\infty) e^{-\ln(2) \left[\frac{(E - I_m^p - \hbar\omega_{\text{Probe}} + DIP_n)}{2\delta} \right]^2} \quad (24)$$

The latter takes into account both the broadenings due to nuclear vibrations, probe pulse bandwidth and the instrument resolution. We also found that the position of the phase jump observed in the calculated photoemission spectra (see Section S2.2) is rather insensitive to changes in the parameter δ in the 1.5 – 3.5 eV range.

S2. Results.

S2.1 First ionization of the neutral species by the x-ray pump pulse: characterization of the mixed state of the cationic system prepared by pump ionization.

Pump ionization is described by directly propagating the initial ground state of the neutral molecule with the full many-body B-spline RCS-ADC(2)x/ADC(2,2) Hamiltonian. Results are shown for the equilibrium nuclear geometry of the Gly I conformer.

In the simulation we used a multicenter B-spline basis (21, 25) characterized by a radial box radius $R_{\max} = 70$, a linear grid in the centre-of-mass expansion (21) with step size $h = 0.3 \text{ a.u.}$ and maximum value of the orbital angular momentum $L_{\max} = 12$. The RCS single-particle

basis set we used consists of the virtual orbitals of an HF calculation performed in the cc-pVDZ GTO basis set, further truncated at the threshold energy of 2 a.u.. The number of open ionic channels included in the calculation (see Eq. (2)) and the dimension of the Hamiltonian matrix in A' symmetry space are $N_{Ionic} = 38$ and $H_{RCS-ADC}^{Maxdim} = 220500$, respectively. The values of the CAP parameters used in this calculation are $\eta = 5 \times 10^{-3}$ and $r_{CAP} = 25$ a.u. The *ab initio* simulation of the pump-step has been performed using a linearly polarized pulse, characterized by a Gaussian temporal envelope, a central frequency $\hbar\omega_{Pump} = 274$ eV, peak intensity $I_{Pump} = 6 \times 10^{15}$ W/cm² and time duration $T_{Pump} \sim 1$ fs (FWHM). Convergence of the results has been obtained by using a time-step $\Delta t = 0.5$ as and a Krylov-space dimension $K = 40$ in the Arnoldi/Lanczos time propagation.

The electronic state of the emerging ionic system has been fully characterized by computing the R-IDM. Fig. S1 shows the calculated degrees of quantum electronic coherence $G_{m,n}$ and the relative phases $\varphi_{m,n}$ between each pair of ionic eigenstates populated by the x-ray pump pulse. The final stationary populations $p_n(\infty)$ of the bound ADC(2,2)-calculated eigenstates of the Gly I cation are also shown in the vertical and horizontal side panels of Fig. S1. In the calculations presented here, all the ionic time-dependent populations $p_n(t)$ have converged to their final stationary value at $t \sim 200$ as after pump ionization. The final photoelectron spectrum resulting from the ionization of neutral glycine by the x-ray pump pulse is also plotted in Fig. S1. It is recovered by convoluting the calculated discrete, final populations of cationic states Gaussian function of FWHM width $\delta \approx 2.5$ eV, which takes into account both the broadenings due to nuclear vibrations, probe pulse bandwidth and the instrument resolution:

$$p_{e^-}^{Pump}(E) = \sum_n p_n(\infty) e^{-ln(2) \left[\frac{(E - \hbar\omega_{Pump} + I_n^p)}{2\delta} \right]^2} \quad (25)$$

In Fig. S1, it is possible to identify islands of strong quantum electronic coherence close to the main diagonal (the highest degrees of generated quantum electronic coherence being ~ 0.95), for ionic states belonging to the 10a' (highlighted in Fig. S1) and 9a' bands. In general, a robust degree of coherence is produced between pair of states with an energy gap up to the value of

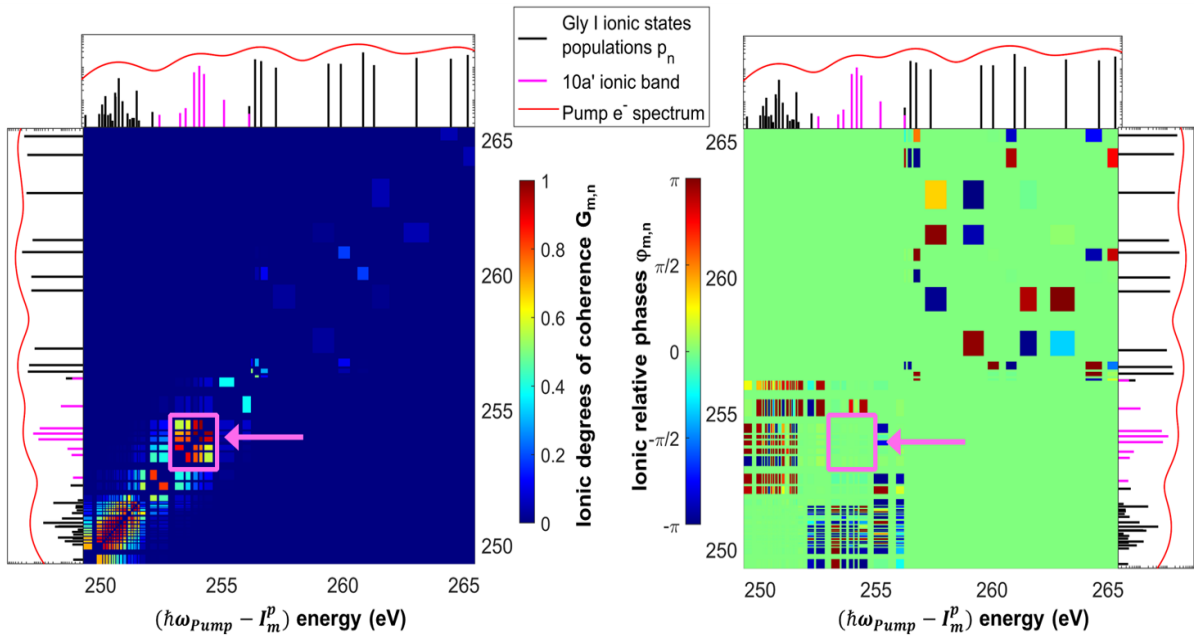


Fig. S1. *Ab initio* TD B-spline RCS-ADC simulation of the pump-induced first ionization of molecular glycine (Gly I conformer). The simulation is performed using the measured FLASH pulse parameters. The interaction between the pump X-ray pulse and the neutral Gly I molecule prepares a cationic system (Gly I^+) in a mixed state characterized by a density matrix. The left panel shows the degrees of quantum electronic coherence $G_{m,n}$ (Eq. (9)) produced between each pair of ADC(2,2)-calculated cationic eigenstates populated by the pump pulse. The relative phases $\varphi_{m,n}$ (Eq. (10)) between each pair of ADC(2,2)-calculated ionic eigenstates are shown in the right panel. The areas corresponding to states of the $10a'$ band are highlighted. The populations of the ionic eigenstates, plotted against the corresponding photoelectron energy $(\hbar\omega - I_m^p)$, are also shown in the vertical and horizontal side panels; the ionic states of the $10a'$ band are highlighted by a different stick colour. The kinetic energy distribution of pump-ionized electrons (Eq. (25)) is also shown in the vertical and horizontal side panels (red curve).

pump-pulse bandwidth, while the coherence produced between different ionic eigenstates with larger energy gaps rapidly decays to very low (< 0.2) values. The results of our *ab initio* simulation of x-ray ionization are in very good agreement with the predictions of the sudden approximation, especially in terms of the relative phases ($\varphi_{m,n} = 0$) and relative populations of the ionic states belonging to the bands which show a breakdown of the MO picture, such as the $10a'$ (and $9a'$) inner-valence ionized band for which the sudden-approximation ansatz can be written as (using Eq. (4)) $|\Phi_{\text{SUDDEN}}^{10a',N-1}\rangle = |(10a')^{-1}\rangle = \sum_m V_{10a',m}^+ |\Phi_{m,\text{Pump-ionized}}^{N-1,\text{RCS}}\rangle$. The good accuracy of the sudden approximation for molecular ionization at x-ray photon energies

is a result of the high (relative to the energy-scale of the bound electrons dynamics) kinetic energy of the photoelectron leaving the molecular region.

S2.2 Second ionization of the cationic species by the x-ray probe pulse: quantum beatings in the time-resolved photoelectron kinetic-energy distribution observable.

Results are calculated for the nuclear equilibrium geometry of the Gly I conformer. X-ray photoionization of the cationic system by the probe pulse is described here by solving Eqs. (13) and (15) for the cases of the three principal quantum-coherent pure-state channels, denoted here as $|\Phi_1^\rho(t)\rangle$, $|\Phi_2^\rho(t)\rangle$, $|\Phi_3^\rho(t)\rangle$, as obtained in Eq. (11) by the purification of the ionic density matrix prepared by the pump pulse. These principal, coherent ionic channels correspond to the coherent superpositions of ionic states in the $10a'$ ($I_{10a'}^p \sim 20$ eV, $r_1 = 0.15$) and $9a'$ ($I_{9a'}^p \sim 23$ eV, $r_3 = 0.09$) bands, respectively, as well as the coherent superposition of the two ionic states consisting of $11a'$ and $12a'$ hole-mixing ($r_2 = 0.13$) at an energy $I_{11a'/12a'}^p \sim 17.5$ eV.

The absolute value of the expansion coefficients of these pure-state channels (in the basis of the 38 ionic eigenstates $\{|\Phi_{m,\text{Pump-ionized}}^{N-1,RCS}\rangle\}$ included in the simulation of the x-ray pump ionization step) as calculated by Eq. (11), are shown in the insets of Fig. S3. The other pure-state channels contributing to the expansion of Eq. (11) are characterized by a negligible quantum coherence in the basis of the cationic eigenstates and therefore do not contribute to the observed oscillations in the photoelectron observables.

In order to illustrate the charge dynamics triggered by the x-ray pump ionization, in Fig. S2 we show the hole densities (defined as the difference between the electron density of the neutral ground state and the one of the pump-prepared correlated ionic state), corresponding to the $10a'$ band coherent ionic channel $|\Phi_1^\rho(t)\rangle$, at two different times, namely immediately after the pump ionization event and 11 fs after it

.

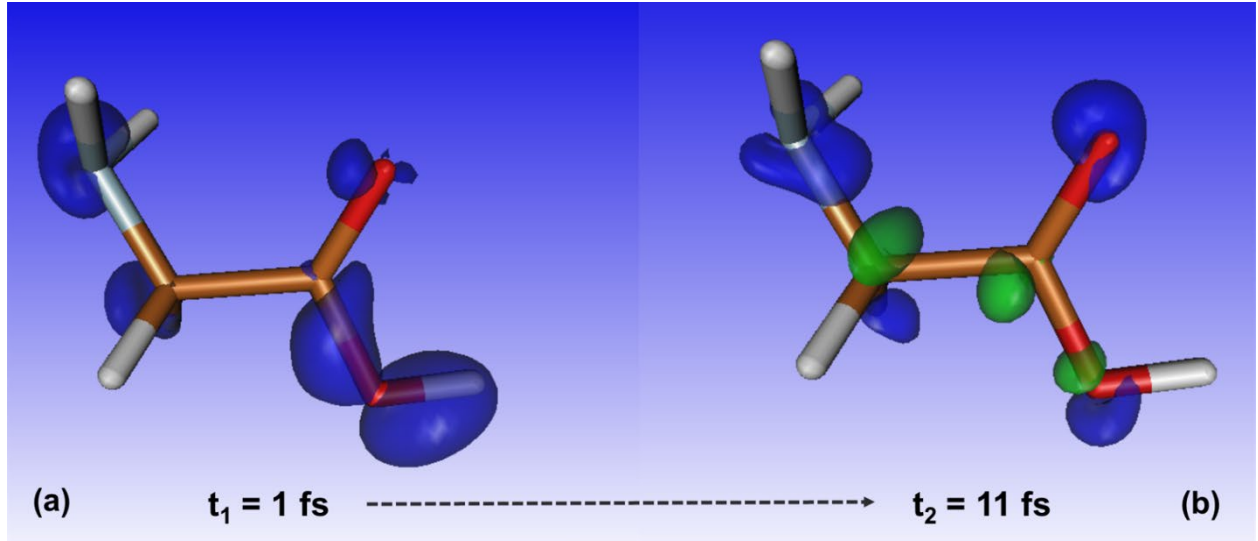


Fig. S2. Hole densities corresponding to the correlated 10a' pure state channel at $t_1 = 1 \text{ fs}$ (a) and $t_2 = 11 \text{ fs}$ (b) after the pump ionization event. The density iso-surfaces displayed are the ones with value 0.015, blue and green colors indicate positive and negative values of the hole density, respectively.

The time propagation is performed by means of the Arnoldi/Lanczos algorithm. During the simulation of the probe step, we have included in the expansion of the many-electron wavefunction Eq. (15) all the open doubly-ionized channels with energy up to 3.5 a.u. The resulting number of open dicationic channels included in the simulation is $N_{\text{Dication}} = 225$. The highest value (among the different molecular symmetry spaces) of the Hamiltonian matrix dimension is $H_{\text{RCS-ADC}}^{\text{Maxdim}} = 1335318$. The other numerical parameters are the same as for the simulation of the pump step (see Section S2.1).

To reduce the demanding computational effort resulting from the size of the Hamiltonian matrix, we employed the following approximation and neglected the interchannel couplings in the continuum between different dicationic channels, i.e. we set

$$\langle \Phi_{\nu,n'}^{N-1} | \hat{H}_{\text{RCS-ADC}}^{N-1} | \Phi_{\mu,n}^{N-1} \rangle = 0, \quad n' \neq n.$$

Fig. S3 shows the relative variation, as a function of the x-ray pump-probe time-delay τ_d , of the separate contributions to the probe-induced electron yield $p_{e^-}^{\text{Probe-pulse}}$ (Eq. (24)) from the three pure-state ionic coherent superpositions associated with the 10a', 11a'/12a' and 9a' bands, respectively. The change of electron yield is plotted relative to the time-delay averaged

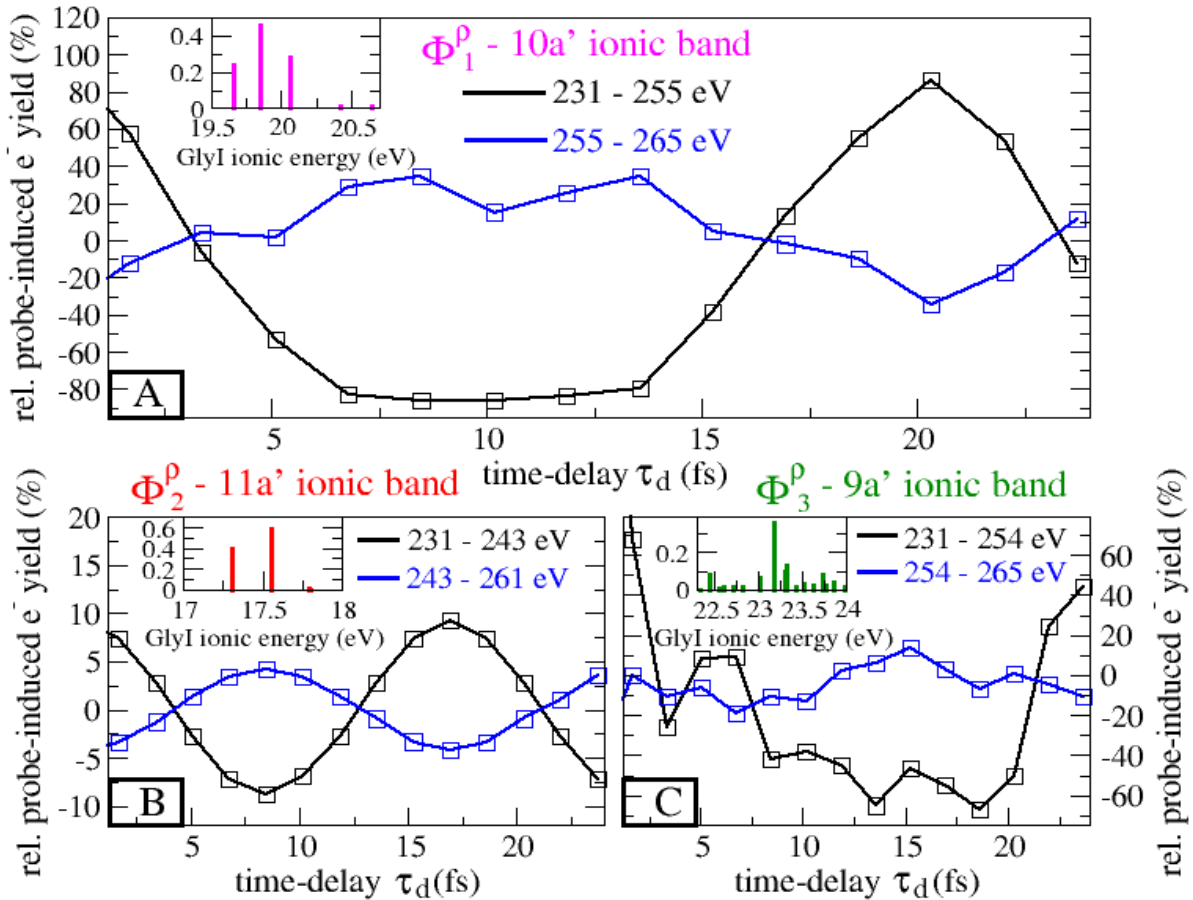


Fig. S3. *Ab initio* TD B-spline RCS-ADC simulation of the interaction between the probe pulse and the pump-prepared cationic system (Gly I conformer). The simulation is performed using the measured FLASH pulse parameters. (A) Relative change of the probe-produced electron yield in the kinetic energy ranges above and below the phase jump, as a function of x-ray pump-probe delay; contribution from the pump-prepared pure-state ionic channel consisting of a coherent superposition of eigenstates in the 10a' ionic band. In both energy ranges the electron yield includes contributions from Auger emission and sequential double ionization as a function of x-ray pump-probe delay. **(B)** and **(C)** – same as **(A)** for the contribution of the pump-prepared pure-state ionic channels consisting of coherent superpositions of eigenstates in the 11a'/12a' and 9a' ionic bands, respectively.

value. Since the time-delay oscillation of the relative change in $p_{e^-}^{Probe-pulse}(E, \tau_d)$ shows, for each coherent ionic channel, a change of phase by π in different regions of the kinetic energy spectrum, we plot the integrated $p_{e^-}^{Probe-pulse}(\tau_d)$ yield in both the kinetic energy ranges above and below the phase jump position resulting from the *ab initio* numerical calculations.

The calculated position of the phase jump for the 10a' and 9a' coherent ionic channels (~ 255 eV) appears shifted to a higher value of the electron kinetic energy with respect to the one observed in the experimental data. This deviation shows that, despite the excellent agreement in capturing at a qualitative level the phase-jump mechanism, the theoretical modelling of the final doubly-ionized states $|\Omega_{n,Probe-ionized}^{N-2,RCS}\rangle$ adopted here does not accurately include the effect of electron correlation in the populated final states of the glycine dication. The part of the spectrum where the phase jump is observed in the experiment is a region of complete breakdown of the MO picture of double ionization, characterized by a high density of doubly-ionized satellite states. As a result, the contribution of 3h1p configurations to the description of the states in this energy region is very strong. Since this contribution is not included here (at the ADC(1) level, 2h configuration mixing is taken into account), the absolute position of the dicationic energy band is not well-captured at a quantitative level, leading to a shift of the predicted phase-jump position.

In both energy ranges the electron yield includes contributions from both the direct sequential double ionization (SDI) by the probe pulse of the cationic states populated coherently by the pump pulse, and the Auger emission from the probe-excited 4a' and 5a' core-ionized Auger channels.

In order to quantify the relative contribution of these two mechanisms, in Fig. S4 we show the relative change, as a function of the x-ray pump-probe time-delay, of the total contribution from the pump-prepared cationic mixed state to probe-induced electron yield in the kinetic energy ranges above and below the phase jump. For comparison, we plot also the isolated contribution due to electrons emitted through Auger-decay. The total spectrum shown in Fig. S4 consists of the incoherent sum of the individual contributions from the 3 coherent pure-state channels shown in Fig. S3. The Auger electron contribution for each coherent channel is calculated as

$$p_{e^{-Auger}}(E) = \sum_n p_n^{2+,Auger}(\infty) e^{-\ln(2) \left[\frac{(E - I_m^p - \hbar\omega_{Probe} + DIP_n)}{2\delta} \right]^2} \quad (26)$$

by integrating the CAP term of the diagonal dicationic density matrix (Eq. (23)) starting from $t = 0.5$ fs after the probe pulse

$$p_n^{2+,Auger}(\infty) = |\rho_{n,n}^{2+,Auger}(\infty)| = \left| \lim_{t \rightarrow \infty} 2 \int_{0.5fs}^t \sum_{\mu,\nu} w_{\nu,\mu} c_{m\mu}(t') [c_{n\nu}(t')]^* dt' \right| \quad (27)$$

The validity of this formula is based on the different time-scales corresponding to direct and Auger electron emission, and by the fact that the photoelectron wave-packet emitted as a result of direct photoionization by the probe pulse is completely absorbed by the CAP within the first 0.3 fs after the probe pulse. The total Auger electron contribution presented in Fig. S4 thus describes the total yield of electrons emitted in the Auger decay of the C(1s) 4a' and 5a' core-ionized states populated by the probe pulse.

The result of Fig. S4 show that, at the photon energy value used in the present experiment, the direct photoionization dominates over the excitation of the intermediate Auger-active core-singly-ionized C(1s) resonances. The calculated Auger signal is indeed about one order of magnitude smaller than the SDI one.

Therefore, the quantum-coherent electron dynamics prepared by the x-ray pump in the cation is imprinted in the direct probe-ionized electron signal, which dominates over the Auger-induced electron signal. Moreover, the results show that the photoelectron signal is more sensitive to the quantum coherence in the 10a' band compared to the coherences produced in the 11a'/12a' and 9a' ionic bands: this is because the pure-state ionic channel consisting of a coherent superposition of eigenstates in the 10a' band is characterized by a higher population weight $r_{10a'} = 0.15$ (see Schmidt decomposition in Eq.(11)), and, as shown in Fig. S3, also gives rise to higher-amplitudes in the calculated oscillation of the electron yield. As a consequence, the position of the phase jump in the total time-delay dependent electron yield is also approximately the same as the one of the 10a' coherent channel alone.

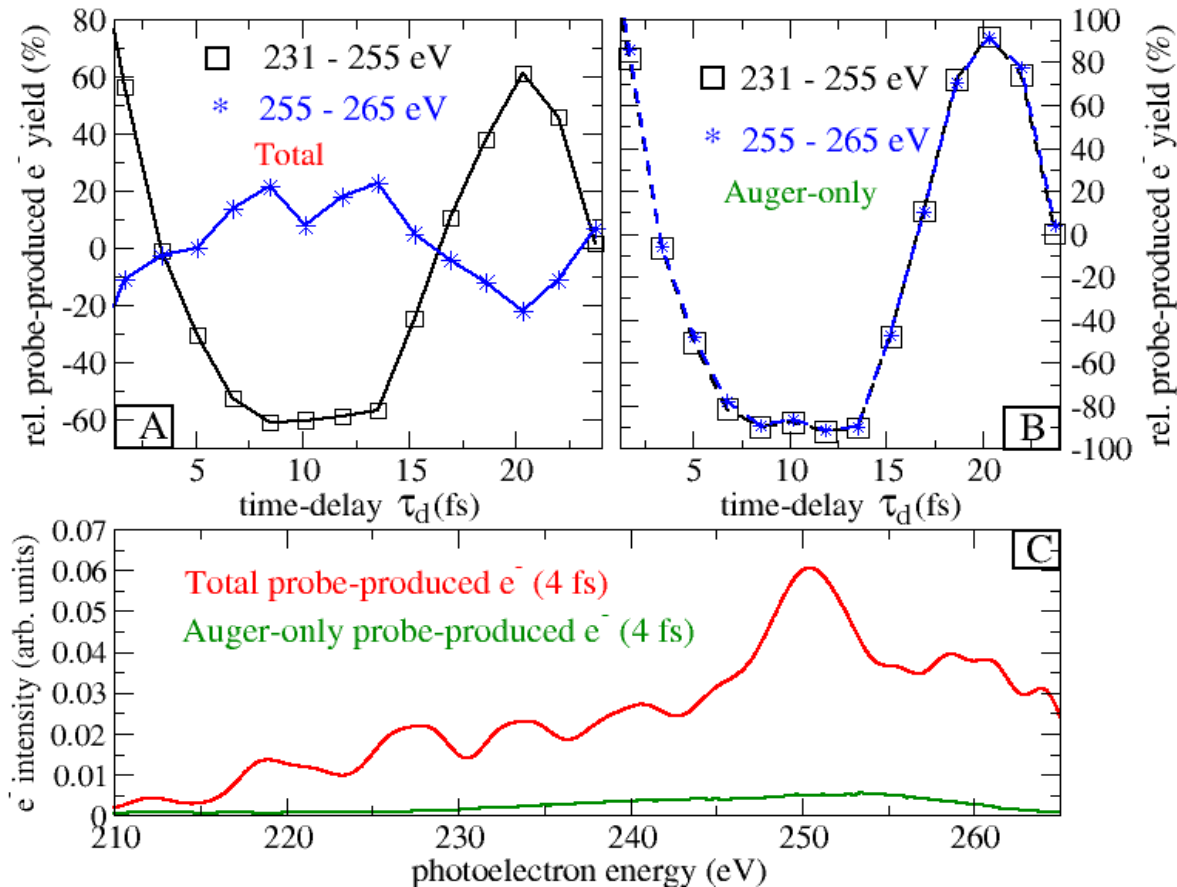


Fig. S4. *Ab initio* TD B-spline RCS-ADC simulation of the interaction between the probe pulse and the pump-prepared cationic system (Gly I conformer). The simulation is performed using the measured FLASH pulse parameters. (A) Relative change of the probe-produced electron yield in the kinetic energy ranges above and below the phase jump, as a function of x-ray pump-probe delay; total contribution from the pump-prepared mixed-state of the ionic system. In both energy ranges the electron yield includes contributions from Auger emission and sequential double ionization as a function of x-ray pump-probe delay. (B) same as (A) for the isolated contribution of Auger electrons, resulting from the decay of the $5a'$ and $4a'$ core-ionized states populated by the probe. (C) Kinetic energy distributions of the probe-induced Auger electrons (green curve) and the complete (Auger + SDI) probe-emitted electrons (red curve); the latter includes the dominant contribution of the photoelectron emitted in the process of (second) direct photoionization of the cationic system by the probe pulse.

S3. Effect of nuclear ground-state geometry distribution: time-dependent survival probability of the pump-prepared mixed state.

Here we analyze the effect of the geometry-spread of the ground state nuclear wavefunction on the survival of the quantum electronic coherences in the $10a'$ and $9a'$ ionized bands. The simulations were performed for and averaged over 201 different nuclear geometries, at which convergence of the calculated ionic density matrix survival probability was found.

S3.1 Numerical procedure.

The entire procedure of the calculation is outlined below. For each and every nuclear geometry, the calculation we performed consists of three elements:

1- Calculation of the bound ionic states of glycine, in the 10a' and 9a' bands energy regions. This calculation was performed at the advanced ADC(2,2) level of theory (24) by using the cc-pVDZ basis set with the virtual orbital space truncated at the threshold energy of 2 a.u. Here, only ionic eigenstates with more than 1% 10a' or 9a' contribution in their full ADC configuration expansion are kept.

2- The pump-prepared initial mixed-state of the cationic system, characterized by the ionic density matrix $\hat{\rho}(t_0)$, is time-propagated by solving the (field-free) time-dependent von Neumann equation (23)

$$\frac{d}{dt} \hat{\rho}(t) = -\frac{i}{\hbar} [\hat{H}_{ADC(2,2)}^{N-1,RCS}, \hat{\rho}(t)], \quad (28)$$

$$\hat{\rho}(t) = e^{-\frac{i}{\hbar} \hat{H}_{ADC(2,2)}^{N-1,RCS} (t-t_0)} \hat{\rho}(t_0) \exp^{+\frac{i}{\hbar} \hat{H}_{ADC(2,2)}^{N-1,RCS} (t-t_0)}. \quad (29)$$

For each nuclear geometry, the initial $\hat{\rho}(t_0)$ reduced ionic density matrix is built according to the following criteria, which we name *coherence-corrected sudden-approximation ansatz*:

- The relative populations of the valence ionic eigenstates (both in the 10a' and 9a' bands), as well as the relative phases between each pair of eigenstates, are estimated using the sudden approximation ansatz to model the ionization of neutral glycine by the pump pulse. Therefore, each ionic eigenstate has a population proportional to the weight of the simple one-hole configurations in their ADC configuration expansion, and the relative phases are 0.
- We assume a degree of quantum coherence different from zero only between ionic eigenstates of the same symmetry, and consequently do not include ionic states of a'' symmetry in our description. Assuming a coherence different from zero only between

ionic states of the same symmetry implies that the direction of the first emitted photoelectron is either not measured or integrated out in the analysis of the experimental data. At a theoretical level, it corresponds to calculating the ionic density matrix by tracing the full N-electron neutral wavefunction over the spatial-symmetry quantum numbers of the photoelectron.

Finally, for each pair of coherently populated ionic eigenstates, the degree of coherence is further decreased (from the initial value of 1) in order to take into account the effect of their energy separation, the bandwidth and profile of the pump pulse. Therefore, the off-diagonal matrix elements $\rho_{m,n}(t_0)$ of the ionic density matrix are modified according to

$$\rho_{m,n}(t_0) = \rho_{m,n}^{Sudden} e^{-\ln(2)\left(\frac{E_m - E_n}{E_{Band}}\right)^2}, \quad (30)$$

which provides a reliable estimate of the initial ionic density matrix prepared as a result of ionization by a 274 eV x-ray Gaussian pump pulse of bandwidth E_{Band} .

The validity of this ansatz is confirmed, at the nuclear equilibrium geometry, by the *ab initio* results of Fig. S1.

3- Given the density matrix $\hat{\rho}(t)$, the survival probability of the time-dependent quantum state is calculated as the fidelity between the quantum states described by the density matrix $\hat{\rho}(t)$ and the initial density matrix prepared by the pump $\hat{\rho}(t_0)$

$$F(t) = \left(\text{Tr} \left[\sqrt{\sqrt{\hat{\rho}(t)} \hat{\rho}(t_0) \sqrt{\hat{\rho}(t)}} \right] \right)^2. \quad (31)$$

S3.2 Nuclear geometry sampling.

The optimization of the equilibrium geometry $\{\vec{R}_n\}_0$ and the calculation of the normal-mode frequencies were computed at the coupled-cluster singles and doubles (CCSD) level of theory in a cc-pVTZ basis set, using the MOLPRO quantum chemistry package (27); the different nuclear geometries were sampled in the configuration space according to a probability

distribution given by the Wigner distribution, integrated over momenta, corresponding to the nuclear ground-state (GS) wavefunction, i.e. $|\Lambda_{GS}^{Nuclear}(\{\vec{R}_n\})|^2$. The latter was calculated within the harmonic oscillator approximation (around the equilibrium geometry) of the potential energy surfaces. Therefore, the ensemble of geometries was calculated using a product of normal Gaussian distributions, each one corresponding to the respective vibrational normal mode considered. Only vibrational normal modes that conserve the molecular symmetry of the equilibrium geometry (C_s point group) were considered. Monte Carlo integration of the time-dependent survival probability curves over different nuclear geometries $\{\vec{R}_n\}$ was performed. The aforementioned procedure describes the effect of the spread of the GS nuclear wavefunction on the observed coherent electron dynamics. Vibrational dynamics is not included in the simulations.

S3.3 Results.

Fig. S5 shows the geometry-averaged, time-delay-dependent survival probability of the ionic density matrix prepared by the x-ray pump ionization. Results are presented for the two conformers Gly I and Gly III, as well as for three different statistical mixings of the populations of the two conformers in the sample.

The results for both the singly-ionized Gly I conformer and the averaged abundance-weighted contribution of the two (Gly I and Gly III) conformers, show that it is possible to discern an oscillation with a ~ 20 fs period in the time-dependent survival probability of the cationic mixed state prepared by the pump ionization. The overall agreement with the experimental results is excellent in terms of the oscillation period and it provides strong evidence in support of the presence of an electronic coherence-driven oscillation characterized by a period of ~ 20 fs and whose coherence partially survives the nuclear GS distribution averaging.

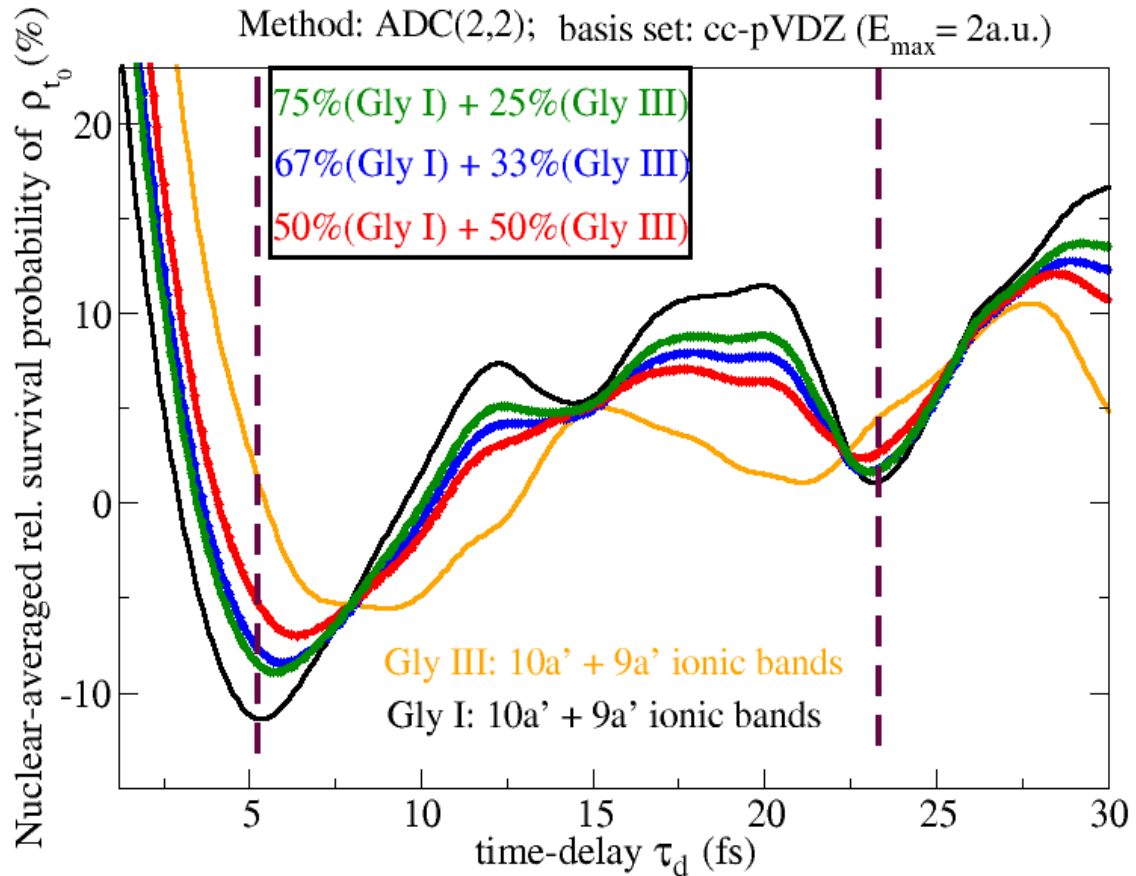


Fig. S5. Time-dependent survival probability of the pump-prepared ionic density matrix in the subspace of ionic eigenstates consisting of the 10a' and 9a' ionic bands. The result of Eq. (31) has been averaged over the nuclear ground-state geometry distribution for both the Gly I and Gly III conformers, as well as for three different statistical mixtures of the two.

Here it is important to note that, whereas both the time-dependence and the temporal resolution of the measured physical observable does in principle present deviations from the calculated survival probability, the robustness of the latter with respect to the nuclear geometry averaging provides a probe-free demonstration of the survival of quantum electronic coherence on the tens-of-femtosecond time-scale in this system.

Regarding the profile of the oscillation, neither the theory results nor the bare experimental data points show a simple, perfectly singled-period oscillation. Moreover, the amplitude of the calculated oscillation is around 10% (measured against the time-delay averaged value), and therefore smaller than the experimentally measured one which ranges from 15% up to 30%.

The observed difference in the relative amplitude of the oscillations has to be considered remarkably small, and thus supportive of the presented experiment's interpretation, especially considering the potential theoretical sources of discrepancy (in addition to the experimental errors), which include:

- Errors due to the use of a truncated single-particle basis set in the calculation of the $10a'$ and $9a'$ ionized states at the ADC(2,2) level of the ADC hierarchy. This can in principle have an appreciable impact on the observed discrepancy, as it can lead to relative errors in the excited ionic states expansions and consequently in the energy gaps between different ionic eigenstates as well as in the geometry of the corresponding potential energy surfaces.
- Deviations, as a function of the nuclear geometry, of the relative ionic populations and ionic coherences, estimated by means of the procedure outlined above, with respect to the pump-prepared ones. The vertical ionization probabilities by the pump could potentially present deviations from the theoretically estimated one for the states involved, depending on the vertical ionization energies at different geometries.
- The effect of phenomena not-included in the present analysis:
 - i. the symmetry-breaking vibrational normal modes.
 - the ionization-induced nuclear motion.
 - ii. Given the relatively high temperature of the molecular sample used in the experiment, contributions from excited vibrational states could also play a non-negligible role.